Experimental hydrothermal alteration of basaltic glass with relevance to Mars.

C. Sætre[a,c]*, H. Hellevang[a,d], L. Riu[b], H. Dypvik[a,c], C. Pilorget[b], F. Poulet[b], and S. C. Werner[a,c]

[a]University of Oslo, Department of Geosciences, P.O box 1047 Blindern, N-0316 Oslo, Norway

[b]Institut d'Astrophysique Spatiale, Bâtiment 121, CNRS/Université Paris-Sud, 91405 Orsay Cedex, France

[c]University of Oslo, Centre for Earth Evolution and Dynamics, P.O box 1028 Blindern, N-0315 Oslo, Norway

[d]The University Centre in Svalbard (UNIS), Pb. 156, N-9171 Longyearbyen, Norway

*Corresponding author e-mail address: christian.satre@geo.uio.no

Abstract

Phyllosilicates, carbonates, zeolites and sulfates on Mars give clues about the planet's past environmental conditions, but little is known about the specific conditions in which these minerals formed within the crust and at the surface. The aim of the present study was to gain increased understanding on the formation of secondary phases by hydrothermal alteration of basaltic glass. The reaction processes were studied under varying conditions (temperature, pCO_2, water:rock ratio, and fluid composition) with relevance to aqueous hydrothermal alteration in fully and partly saturated martian basalt deposits. Analyses made on reaction products using X-ray diffraction (XRD) and Scanning Electron Microscope (SEM), were compared with Near Infrared Spectroscopy (NIR) to establish relative detectability and spectral signatures.

This study demonstrates that comparable alteration minerals (phyllosilicates, carbonates, zeolites) form from vapor condensing on mineral surfaces in unsaturated sediments and not only in fully water saturated sediments. In certain environments where water vapor might be present it can alter the basaltic bedrock to a suit of authigenic phases similar to those observed on the martian surface. For the detection of the secondary phases, XRD and SEM-EDS were found to be superior to NIR for detecting and characterizing zeolites. The discrepancy in detectability of zeolites between NIR and XRD/SEM-EDS might indicate that zeolites on Mars are more abundant than previously thought.

INTRODUCTION

Observations made by the two imaging orbiting spectrometers OMEGA (Observatoire pour la Minéralogie, l'Eau, les Glaces et l'Activité; Bibring et al. 2004) and CRISM (Compact Reconnaissance Imaging Spectrometer for Mars; Murchie et al. 2007) have revealed widespread occurrences of phyllosilicates on Mars (Poulet et al. 2005; Mustard et al. 2008). Timing of phyllosilicate formation ranges from Noachian (>3.7 Ga) to Hesperian (3.7–3.0 Ga) or even younger (Dehouck et al. 2010; Grindrod et al. 2012; Mangold et al. 2012). Additionally, the Curiosity rover has detected ferrian saponites and Al-rich smectites in abundances up to ~20 wt% in the fluvio-lacustrine Murray formation of Hesperian age (Vaniman et al. 2013; Bridges et al. 2015; Bristow et al. 2015; Schwenzer at al. 2016). More

than 50% of **detected** martian clay minerals and the majority of zeolite detections are associated with impact structures (Carter et al. 2013). Iron/magnesium smectites and chlorite dominate the phyllosilicate mineral assemblages with occasional minor quantities of analcime, silica, serpentine and mica (Ehlmann et al. 2011a, 2011b; Carter et al. 2013).

Several studies have suggested that secondary minerals have been formed by impact-triggered hydrothermal systems in martian craters (Tornabene et al. 2009; Fairén et al. 2010; Marzo et al. 2010; Mangold et al. 2012; Carrozzo et al. 2017). This has been inferred from occurrences of mineral assemblages associated with impact-induced hydrothermal systems in terrestrial craters (e.g., Hagerty and Newsom 2003; Osinski 2005). Additionally, modeling shows that long-lived hydrothermal systems can be generated if sufficient water or ice is present in the subsurface (Newsom 1980; Rathbun and Squyres 2002; Abramov and Kring 2005; Schwenzer and Kring 2009), with upwelling of water and vapor (Abramov and Kring 2005; Mangold et al. 2012; Marzo et al. 2010).

Low temperature weathering has also been proposed as a source for locally formed phyllosilicates, e.g., in Valles Marineris (Le Deit et al. 2012) and Gale Crater (Retallack 2014). Moreover, in proposed weathering settings Al-phyllosilicates (montmorillonite, beidellite and kaolinite) commonly overlie Fe/Mg-phyllosilicates (nontronite and saponite), reflecting varying pH conditions and availability of meteoric water through time (Ehlmann et al. 2011b; Le Deit et al. 2012).

Salts are common within the martian soil observed by the Viking landers and might be sourced from chemical weathering (Clark and Van Hart 1981) or from fluids related to impact-induced hydrothermal events (Newsom et al. 1999). Global warming by high CO_2 pressures cannot alone explain the presence of surface liquid water on Mars (Forget et al. 2013; Bristow et al. 2017), but mean surface temperatures reaching 273 K may be possible assuming an atmosphere having CO_2 pressures of 1.25–2 bar and 2–10% CH_4 or H_2 (Wordsworth et al. 2017). Fairén et al. (2009) demonstrated that reaction waters produced during weathering of basaltic bedrock could be stable at temperatures of 273 K due to lower melting point and reduced equilibrium vapor pressure.

Liquid water together with a CO2-rich atmosphere is favorable for basalt alteration and the formation of authigenic carbonate, zeolite, and phyllosilicate minerals, as observed in several experimental and geochemical modeling studies (e.g., McGrail et al. 2006; Goldberg et al. 2008; Viennet et al. 2017; Gaudin et al. 2018). Even though there was an active water system on Mars in the Noachian and Early Hesperian (Di Achille and Hynek 2010) and climate models suggests a CO_2 containing atmosphere only small abundances of carbonates have been observed. Fairén et al. (2004) showed that the absence of carbonates may be explained by water pH conditions below 6.2 inhibiting carbonate formation. Hydrothermal experiments and reaction path modeling performed by Viennet et al. (2017) showed a correlation between di- and trioctahedral smectites and dissolved CO_2. The trioctahedral varieties were favored at low levels of dissolved CO_2 and alkaline conditions. Additionally, under the experimental conditions applied, their reaction path model showed formation of Ca-zeolites at pH $\geq$ 7.2.

The aims of this study were to compare alteration in fully and partly water saturated basaltic rock soils, and to compare X-ray and optical detection methods for these secondary phases. The experimental setups used were designed to assess the role of contrasting water:rock (W:R) ratios in the formation of secondary phases, as little is known about the W:R ratio during martian hydrous alteration. Two endmember water:rock ratios were investigated: fluid-dominated (W:R ratio of 10) and rock-dominated systems (low W:R ratio). The latter involved reacting the basaltic rock powder with a water-saturated vapor. In addition, varying levels of dissolved CO_2, and saline concentrations (1–4 molar concentration NaCl), were used to investigate how these affect the secondary mineral assemblage. The

reactors were either flushed with 1 bar CO_2 or equilibrated with atmospheric CO_2 pressures. Initial levels of dissolved CO_2 were chosen to supplement previous studies that had been performed at higher CO_2 pressures (Hellevang et al. 2013). A reaction path model was constructed to increase the understanding of the fluid-dominated systems. The XRD and SEM-EDS results were compared with the Near Infrared Spectroscopy (NIR) data in order to establish the signatures and relative detectability of the reaction products.

MATERIAL AND METHODS

Basalt

A tholeiitic basaltic glass from Stapafell in Iceland was used in all the experiments. This glass is chemically similar to common martian basalt compositions (McSween et al. 2009) and therefore serves as a good analog for studying the alteration of martian basalts. This basalt has previously been described and used in several kinetic and experimental studies (e.g., Gysi and Stefánsson 2011, 2012a; Hellevang et al. 2013; Galeczka et al. 2014; Hellevang et al. 2016; Viennet et al. 2017), but before only reacted at fully saturated conditions. Major element composition of the original basalt is presented in Table 1. A glass phase was preferred due to its abundant formation during impact processes (Newsom 1980) and higher dissolution rates compared to crystalline basalt at alkaline conditions and temperatures >50°C (Gudbrandsson et al. 2011), which was advantageous for ensuring formation of secondary minerals within the timeframe of the experiments.

Prior to the experiments, the basaltic glass was cleaned by overnight soaking in a deflocculating agent (sodium carbonate solution) to remove any clay minerals. After this the basalt was cleaned by repeated ultrasonic dispersion treatment in deionized water for 12 minutes per round, and repeated flushing with deionized water to remove remains of the sodium carbonate solution. After washing and drying the basaltic material was crushed to a rock powder in two steps: grinding in an agate mortar with acetone until a particle size of <0.5 mm was attained, then 3 grams of mortared material was combined with 7 ml of ethanol in an agate mill (McCrone Micronizer Mill) and ground for 12 minutes. The very small resultant particle size provides a large total reaction surface, promoting dissolution and precipitation reactions.

Experimental procedure

In order to study the alteration of the basalt and the specific conditions under which secondary minerals form on Mars, at saturated and unsaturated mineral soil conditions, several hydrothermal alteration experiments were set up, with different initial conditions, as listed in Table 2.

A first series of experiments (I, to V, Table 2) were designed to test water-basalt and CO_2-water-basalt alteration at temperatures of 120°C and 200°C. Temperatures were chosen to ensure parent rock dissolution and formation of secondary phases within the experimental periods of 21 days (I to VI) and 32 days (V). Alteration with contrasting water:rock ratios (W:R) was tested using a W:R of 10:1 (fluid-dominated system) and low W:R in experiments where the glass was reacted in the vapor phase (rock-dominated system). In addition, the effects of variation in dissolved CO_2 concentrations at saturated atmospheric and 1 bar pressures were applied to test CO_2 conditions lower than those employed in earlier experiments by Hellevang et al. (2013).

The first series of experiments was performed in closed system 600 ml Hastelloy ® Parr© reactors. Micronized basaltic glass (10 g) was placed in the bottom of the reactor and

mixed with MilliQ-water to obtain a water:rock ratio of 10:1. In the same reactor basaltic glass was placed in an elevated container to investigate the alteration process between condensed vapor droplets under rock-dominated conditions that provided a very low W:R. In this container 1 g of material was used (experiment IIb and Vb, Table 2). A redesigned container allowed for 10 grams of material for the remaining vapor phase experiments. To saturate the water with 1 bar of CO_2 the reactor was purged with CO_2 for 5 minutes at 25°C through a dip tube in the liquid. Deionized water (MilliQ-water) was used in both experiments, but in CO_2-charged experiments it was O_2 depleted before being added to the reactor. Oxygen depletion was done by transferring deionized water to a vacuum container placed in an ultrasonic bath for 5 minutes. Experiments were performed at vapor saturation pressure. Temperature and pressure were monitored throughout the experiments.

A second set of experiments (VI, Table 2) was performed to investigate saline water/basalt interaction as salts have been identified in martian soils (Clark and Van Hart 1981). A temperature of 150°C was chosen, within the temperature range of the first set of experiments. 3 g of basaltic glass was placed in a small, 20 ml, Teflon-lined vessel to ensure extraction of sufficient amount of the produced clay size fraction. One reference experiment was performed using only deionised water (MilliQ-water). Three salt-containing experiments, using 1, 2, and 4 M NaCl solutions, were done. The salt solutions were made by mixing NaCl with deionized water (MilliQ-water) to the desired concentration. The basaltic glass was loaded into the reactor and fluid was added to the top of the reactor. After adding the liquid the reactors were closed and placed in a stove at 150°C for 42 days. At the end of experiments all reactors were checked for leakages by assessing the reactor water levels.

Analytical procedures

Whole rock and clay mineral assemblages of all experimental products were identified by XRD analysis using the Bruker D8 Advance instrument at the Department of Geosciences at UiO, using CuKα radiation (40 kV, 40 mA, and wavelength of 1.5418 Å). Spectra were gained using a variable slit, step size of 0.031° 2θ, and count time of 1.25 s (bulk) and 0.3 s (clay fraction) in the intervals 2–65° 2θ and 2–55° 2θ for whole rock and clay fraction samples, respectively. Whole rock samples were in addition analyzed in the 58–65° 2θ range with decreased step (0.02° 2θ) and increased count time (5.0 s) to examine randomly oriented phyllosilicate (060) peaks. Mineral identification of randomly oriented whole rock samples was done using the BRUKER DIFFRAC.EVA software and the Powder Diffraction File-2 2002 mineral database (ICDD). Dioctahedral and trioctahedral smectite varieties were determined by position of the randomly oriented (060) peaks following Moore and Reynolds (1997). Quantification of the mineral phases was done by Rietveld refinement using the PROFEX software (Doebelin and Kleeberg 2015). The amorphous phase was excluded from the quantification and the results are semi-quantitative.

Clay fraction separation of the reaction products was done by gently crushing the experimental material in an agate mortar before soaking overnight in sodium carbonate solution followed by ultrasound dispersion for 12 minutes to avoid flocculation, before gravity settling of material larger than 2 μm. In experiments IIb, Vb, and VI a small part of the clay fraction was removed prior to bulk analysis due to the small sample size. Oriented XRD samples were prepared using the filter transfer method as described by Moore and Reynolds (1997). All oriented samples were analyzed after each of the following four steps: air dried, overnight exposure to ethylene glycol (EG) at 60°C, and 1 hour heating at 350°C and then at 550°C. Clay minerals were identified by (00*l*) peak positons and responses to the above treatments. Full pattern modeling of all clay fraction patterns to obtain a better

understanding of clay mineral structures and relative mineral quantities was done in NEWMOD (Reynolds and Reynolds 2012).

The powdered material used for XRF was heated overnight at 120°C prior to weighing and heating to 1050°C for 1 hour to release volatiles. Powder and flux was mixed at a ratio of 1:10 before heating and fusion on the Panalytical Eagon 2 instrument. XRF analysis was carried out at the Department of Geosciences, UiO, using a Panalytical Axios Max Minerals fitted with a 4 kW rhodium tube. Quantification was performed using the Panalytical SuperQ version 5.1B software.

To obtain high magnification images and mineral chemistry, experiment reactants and products were studied using a Hitachi SU5000 FE-SEM (Schottky FEG) scanning electron microscope (SEM) equipped with a Dual Bruker XFlash30 Energy Dispersive X-ray Spectroscopy (EDS) system located at UiO.

Water composition analysis was done at UiO either by colorimetric analysis using an AutoAnalyzer 3 or by ICP-MS using the Bruker Aurora Elite equipped with an ESI oneFAST sample introduction system using a 500 µl loop and a Cetac ASX-520 auto sampler.

Total carbon (TC) analysis was done by Applied Petroleum Technology AS using a Leco SC632 instrument by heating the crushed sample to 1350°C in a pure O_2 atmosphere and measuring the CO_2 content in an infrared cell.

The NIR reflectance spectra measurements were carried out using a PerkinElmer FTIR spectrometer at L'Institut d'Astrophysique Spatiale (IAS/Orsay). The instrument has a spot size of ~500 µm, spectral resolution of 1 cm^{-1}, and spectral range from 1 to 4 µm with a spectral sampling of 0.4 nm. The sample measurements were acquired under ambient conditions. Data were calibrated prior to analysis to derive reflectance spectra of the samples, using an Infragold and a Spectralon 99% from Labsphere.

Major secondary minerals were identified with NIR by their distinctive absorption bands (in µm); phyllosilicates (1.41, 1.91, 2.26, 2.32, and 2.34); zeolites (1.41, 1.47, 1.79, 1.91, 2.925, and 3.09); and carbonates (3.35, 3.48, and 3.98). Absorbed H_2O and/or structurally bound OH- produces fundamental and overtone vibration absorption in the 1.2–4.0 µm spectral range. Adsorbed H_2O yields a sharp band at 1.9 µm (Poulet et al. 2005) and a broad and possibly deep band at 3.0 (Jouglet et al. 2007). Primary minerals such as pyroxene and olivine are easily identified in the NIR wavelength range due to their broad signature in the 1.0 to 2.5 µm region. A spectral ratio (altered sample/original basalt) was used to enhance features in samples where absorption signatures were weak.

Reaction path modeling

Reaction path modeling was done using the geochemistry program PHREEQC v3 (Parkhurst and Appelo 2013) together with the phreeqc.dat thermodynamic. Mineral phases that were not included in the phreeqc.dat thermodynamic database were added from the llnl.dat database (also included with the software), and data in Gysi and Stefánsson (2011). Mineral phases allowed to form according to the local equilibrium assumption (Helgeson 1968) are listed in Table 3. The vapor phase was defined using the PHREEQC v3 GAS_PHASE option and solved with a constant-volume flash algorithm (0.5 l gas in equilibrium with 0.1 l of aqueous solution). The internal Peng-Robinson equation of state (Peng and Robinson 1976) provided accurate estimates of gas phase partial pressures and fugacities. The chemistry of the reacting basaltic glass ($Na_{0.072}K_{0.007}Fe_{0.193}Mg_{0.318}Al_{0.365}Ca_{0.259}P_{0.0037}SiO_{3.526}C_{0.078}$, Table 3) was that estimated from XRF (Table 1) data but also included carbon according to the amount measured in the glass. The total amount reacted (0.0792 mol/0.1 l of aqueous solution) corresponds to the 10 g used

in each of the laboratory experiments. Simulations were done with atmospheric and 1 bar pCO_2, and at 120 and 200°C.

RESULTS

Initial basalt

X-ray diffraction studies of the original basaltic material reveal that it consists primarily of an amorphous phase in addition to minor quantities of crystalline forsterite and pyroxene (Fig. 1). A mineral at 3.33Å could not be identified, but may be graphite (quartz with the same d-spacing is not likely). SEM studies of the primary glass, prior to sample preparation, show smooth surfaces without visible signs of alteration. Additionally, the basalt contains a TC of up to 0.74 wt% (Table 1).

Experiments Ia, IIIa, and Va: fluid dominated, air atmosphere

After 3 weeks of reaction at 120°C the whole rock XRD diffractogram was similar to the original basalt and no peaks of secondary phases were detected (Ia, Table 4). In contrast, a smectite phase was observed by SEM coating the original glass. The formation of a clay phase was supported by NIR reflectance spectra with one weak hydration feature (1.9 μm) associated with phyllosilicates (Ia, Figs. 2A and B).

An increased temperature of 200°C (IIIa, Table 4) gave formation of zeolites and clays as the main secondary phases. Two zeolite species were identified by XRD: a Ca-zeolite as the most abundant, having a best match for wairakite ($Ca(Al_2Si_4O_{12}) \cdot 2H_2O$), and a minor abundance of analcime ($Na(AlSi_2O_6) \cdot H_2O$) (Table 4, Figs. 3B and 4C). EDS analyses indicated non-ideal zeolite compositions with absence of zeolites with pure Ca-zeolite or Na-zeolite compositions. The broad and deep absorption feature centered in the 3 μm region (IIIa, Fig. 2E) attests to hydration of the analyzed material. However, the origin of this hydration has multiple causes, including adsorbed water and the band was also detected in the unaltered material. In addition, a 2.6 μm shoulder and subtle features at the 2.925 μm and 3.09 μm bands, characteristic of zeolites, were detected. With the exception of the 2.6 μm shoulder, the signatures were weak and not well defined.

The clay phase observed at 200°C is interpreted as smectite due a shift of the d(001) peak to lower angles (16.7 Å) after ethylene glycol (EG) treatment, and collapsed to approximately 9.6 Å after heating to 550°C. Modelling of the smectite phase produced a best fit for a trioctahedral smectite with a basal spacing of 16.5 Å. Combined with the position of the randomly oriented (060) peak at ~1.54 Å (as in Fig. 3D) and rational spacing of the (00*l*) peaks it was interpreted as a saponite without interstratification. Additionally, EDS analysis indicated substitution of Fe for Mg. There are morphological differences between the top and bottom of smectite crystallites. The top shows characteristic honeycomb morphology whereas the bottom is flat and without structure (Fig. 4C). The presence of the trioctahedral saponite was supported by NIR analyses with absorption features at 2.32 μm and the general clay hydration features at 1.4 μm and 1.91 μm (IIIa, Fig. 2A). The presence of additional and deeper absorption bands at 200°C compared to 120°C indicates stronger alteration at elevated temperature. Additional features at 2.25 μm and 2.34 μm were present for the 32 day experiments and these can be attributed to dioctahedral chlorite and/or smectite, and trioctahedral chlorite, respectively. Moreover, the deepest 2.25 μm absorption band was observed for the Va experiment (Fig. 2B). Possible chlorite minerals where observed by SEM studies, but XRD analysis of the sample did not show the presence of chlorite, indicating abundance below the XRD detection limit.

Dissolved carbon in the basalt (Table 1) resulted in minor calcite formation at 200°C indicated by XRD and the absorption bands at 3.35 μm and 3.98 μm in NIR. The absorption bands were deepest with 32 days experimental run-time (Va, Fig. 2G).

Experiments Ib, IIIb, and Vb: rock dominated, air atmosphere

No secondary phases were observed by whole rock XRD after 3 weeks reaction time at 120°C (Ib, Table 4). However, SEM analysis displayed formation of an unidentified mineral, possibly a zeolite, consisting of intergrown fibres and a grain coating smectite (Figs. 4A and B). No metal-OH bonds were observed by NIR and the overall shape was similar to the unaltered primary basalt (Ib, Fig. 2C).

At a temperature of 200°C, according to whole rock XRD, smectite constituted the most abundant secondary mineral in addition to a minor occurrence of the Ca-zeolite scolecite (IIIb, Table 4). No definite signatures of zeolites were present in the NIR reflection spectra (IIIb, Fig. 2F). Moreover, a small amount of calcite was observed, both by XRD and by the NIR 3.98 μm absorption band (Fig. 2H), which relates to the initial carbon in the basalt. The clay phase was interpreted as a saponite based on both XRD and NIR analyses. A weak feature at 2.25 μm in the NIR spectra (Figs. 2C and D) was attributed to AlFe- or AlMg-OH bonds in dioctahedral chlorite and/or smectite. Additionally, a minor discrete chlorite phase was identified by XRD which in NEWMOD produced a best fit for an interstratified trioctahedral R0 chlorite (0.9)/smectite (C/S). In SEM studies the C/S displayed small straight platelets coating the original basaltic grains (Fig. 4D). The 2.34 μm absorption band related to trioctahedral chlorite was not present.

Experiments IIa and IVa: water dominated, CO_2-H_2O atmosphere

Clays and zeolites were the principal phases at 120°C and 200°C according to XRD (IIa and IVa, Table 4) indicating a marked increase in dissolution and precipitation reactions with increased dissolved CO_2 content. The dominant zeolite phase identified by XRD was a Ca-zeolite, followed by less abundant analcime. NIR showed subtle absorption bands of zeolites, but the specific type(s) could not be identified. The most abundant clay mineral was identified as saponite based on concordant XRD (Figs. 3C and D) and NIR analysis. Moreover, the deepest absorption bands associated with phyllosilicates, compared to all samples, were observed for the 200°C case. Additionally, a small 2.25 μm absorption feature was also present, related to dioctahedral smectite or chlorite. But the 2.34 μm chlorite band was not present. A minor chlorite phase was observed by SEM, but at abundances below XRD detection limits.

Carbonates formed with calcite as the common species. Position of the (104) calcite peak in XRD diffractograms located at ~3.03 Å indicates a low-Mg calcite (e.g., Zhang et al., 2010). No typical NIR signatures attributable to carbonates were detected at 2.3 and 2.5 μm. Distinct detections associated with carbonates were made in the region 3.2–4.0 μm, namely at 3.35, 3.48, and 3.98 μm (IIa and IVa, Fig. 2G). These absorption features were more subtle at 200°C compared to 120°C. It should be noted that in this range (3.3–3.6 μm) the spectra were likely disturbed by organic compounds (e.g., PHAs: polyhydroxyalkanoate) due to sample preparation or transportation. Their presence made the identification of the carbonate signatures at 3.35 μm and 3.48 μm more difficult due to band overlap. The feature at 3.98 μm appeared undisturbed and reduced the carbonate detection ambiguity at an excellent signal-to-noise ratio of the spectra.

Experiments IIb and IVb: rock dominated, CO_2-H_2O atmosphere

Clay minerals (saponite) and carbonates were the main secondary phases revealed by XRD at 120°C (IIb, Table 4, Fig. 3A). No definite zeolites were detected at 120°C by XRD, though SEM studies showed the presence of a possible zeolite with an elongated tabular crystal form. Analysis of the mineral by EDS was not possible, leaving it as an unidentified zeolite (IIb, Table 4). At increased temperature of 200°C the diffractogram changed significantly, attesting a larger degree of dissolution of the primary basalt and precipitation of secondary minerals. Here, only a Ca-zeolite was identified by XRD, in SEM it showed euhedral crystals with clean crystal faces, occasionally overgrowing calcite (Fig. 4E). Based on XRD and NIR the clay phase was identified as the trioctahedral saponite, additionally a minor absorption feature (2.25 μm) related to dioctahedral smectite or chlorite was present in NIR (IIb and IVb, Figs. 2C and D). A possible chlorite mineral was additionally observed by SEM studies.

Calcite was detected at 120°C and 200°C, in addition to aragonite in the high temperature case (IIb and IVb, Table 4, Fig. 4F). The 3.98 μm absorption band in NIR supports formation of carbonates, with no apparent difference in band depth for the two temperatures (IIb and IVb, Fig. 2H).

Experiments VI: liquid dominated, air and saline water

In all the saline experiments a clay phase was identified as the most abundant mineral species (experiment series VI, Table 4). Second to this were Na-zeolite (analcime); its relative abundance from XRD was similar for 1.0 and 2.0 M NaCl, but slightly higher using a 4.0 M salt solution. The NIR absorption band at 1.41 μm shifted towards 1.42 μm with increasing NaCl concentration (Fig. 5A). Moreover, a weak feature was noticed at 1.47 μm. These signatures combined are diagnostic for zeolites. Additional features associated with Na-zeolites at 1.79 μm (Fig. 5A) and 2.54 μm (Fig. 5B) were present and increased with the NaCl concentration. The bands of zeolites centered on 2.925 and 3.09 μm were not clearly detected, possibly due to a broad 3 μm water band which obscures the signatures (Fig. 5B). The zeolite phillipsite formed in the reference sample, but identification and characterization was only possible with XRD.

It should be noted that dissolution and precipitation reactions seemed significantly more progressed in the saline experiments compared to the reference experiment (VI-0), deduced from a lowering of the amorphous bulge between 4.4–2.2 Å and stronger peaks associated with secondary phases. The same trend was observed in NIR with only one hydration feature at 1.91 μm for the reference experiment, whereas with saline reaction fluids several absorption bands related to secondary phases were present.

Smectite was observed as the major alteration phase in the reference experiment as well as in the saline experiments, regardless of salt concentrations. The smectite was interpreted as a saponite, based on absorption bands in NIR and XRD analyses. The 2.25 μm indicates a possible presence of a dioctahedral smectite, with a slight increase in band depth from the 1 to 4 M NaCl solutions (Fig. 5A). EDS measurements of the saponite show common substitution of Fe for Mg, but there was no apparent difference in experimental products between the different salt solutions.

Calcite was observed by XRD in all experiments as a minor phase (Table 4). The relative abundance of calcite was similar in the reference sample and the saline samples. Carbonate band depths (at 3.35 μm, 3.48 μm, and 3.98 μm) increased somewhat with higher NaCl concentration (Fig. 5C). As the source of carbon stems from the original basalt this might indicate somewhat increased basalt dissolution with NaCl concentrations. A minor

additional CO_2 may have been sourced from the reaction fluid which was in equilibrium with atmospheric pCO_2 prior to the experiment.

Water chemistry

Table 5 shows concentrations of selected elements and pH in the reaction water acquired at end of experiment. Using an atmospheric CO_2 saturation all element concentrations increased with temperature (Ia vs IIIa) except for Ca and Si. This is somewhat different for the 1 bar CO_2 saturated experiment where Si decreased while the Ca increased with temperature. The amount of Cl in the solution at atm. pCO_2 and 120°C was 27.8 ppm and increased to 160 ppm at 200°C, and a slight increase in concentration to 179 ppm was observed at 200°C and 1 bar pCO_2. A lower pH was measured for the 200°C (9.9) compared to the 120°C (10.4) (IIIa vs Ia, Table 5) at atmospheric CO_2 saturation. Silica values ranged from 72.55 ppm for IIIa experiment to 198.54 ppm for IIa. Silica was undersaturated with respect to quartz except for IVa experiment (Table 5).

PHREEQC modeling

The model results of the atm. pCO_2 (air) and 1 bar pCO_2 120°C and 200°C scenarios are shown in Fig. 6A to D. The figure x-axis shows % basaltic glass dissolved and the y-axis represents moles minerals formed per 100 ml aqueous solution. One step in the model corresponded to dissolution of 1% of the basaltic glass or 0.1 grams dissolved glass in 100 ml aqueous solution. Mg-phyllosilicates (Mg-nontronite, Mg-saponite, and clinochlore) formed as the largest mineral group in all the scenarios except at 120°C and 1 bar CO_2, where clinochlore was absent. Scolecite formed as the most abundant single mineral and as the only zeolite. The model showed formation of one carbonate mineral, namely calcite, independent of model setup (Fig. 6A to D). All predicted minerals co-precipitated from the first model steps, with the exception of clinochlore which in the 200°C case started forming at an earlier model step than in the experiment at 120°C using atm. pCO_2. The reaction path model indicated a reduced precipitation rate of scolecite if clinochlore was predicted to form, observed as a shift in the curve gradient (Fig. 6). This is supported by the modeled 120°C 1 bar CO_2 scenario where clinochlore was absent and scolecite had a linear growth through the model. A marked shift in the gradient of the calcite curve occurs simultaneously with the onset of clinochlore formation at 200°C and 1 bar pCO_2 (Fig. 6D).

Fig. 6E displays the modeled pH of all scenarios; x-axis shows % glass dissolved and y-axis shows pH. In the atm. pCO_2 scenario, pH rapidly rose from initial levels of 5.6 to 9.5–10.3 depending on temperature, and ended at 10.9 (120°C) and 10.3 (200°C). The initial pH increase was fastest for the 200°C case. For the initial 1 bar pCO_2 scenarios at 120 and 200°C the pH rapidly rose from about 6 up to 7-7.7 and ended at 8.5 (120°C) and 7.9 (200°C) (Fig. 6E). This increase was partly driven by consumption of CO_2 by calcite growth. This shows that the 1 bar pCO_2 case was buffered at lower pH compared to the atm. pCO_2 scenario.

The results of the modeled head-space gas partial pressures (atm.) and dissolved organic carbon (DIC) for the various experiments at temperatures of 25, 120, 150, and 200°C are displayed in Tables 6, respectively. The H_2O pressures (pH_2O) for the different setups were similar for all scenarios, whereas pCO_2 depended strongly on the initial pCO_2 (Table 6). In the atm. pCO_2 scenario pH_2O was large compared to pCO_2 at all temperatures; e.g., at 200°C the pH_2O was 15.5 atm. compared to a pCO_2 of 0.001 atm. Using 1 bar pCO_2, similar values for pH_2O and pCO_2 were obtained at 120°C and at higher temperatures pH_2O dominated with 15.5 atm. while the pCO_2 was 1.38 atm. at 200°C (Table 6).

Table 6 shows dissolved inorganic carbon (DIC) for initial atm. and 1 bar pCO_2. Using an initial 1 bar pCO_2 the DIC was several magnitudes larger (12 mmol/kgw at 200°C) compared to using atm. pCO_2 ($5.96e^{-3}$ mmol/kgw at 200°C) for all modeled temperatures (Table 6).

DISCUSSION

Comparison of NIR and XRD/SEM-EDS

Table 4 provides a comparison of the detectability of phases for the different methods. The results of the combined analyses emphasize the fact that using the present combination of techniques has played a major role in achieving in-depth characterization of the samples. The various instruments each have their limitations. In the NIR measurements the relatively large spot size of ~500µm possibly hampers the detection of microscopic phases due to surface and volume scattering mixing the signal from both altered and non-altered products; some minor phases were only detected by XRD or SEM. NIR spectroscopy also appears less suited for the detection and characterization of zeolites. The challenge here is that the zeolite absorption features between 2.5 µm and 3.5 µm are within the deep and broad 3 µm hydration band, which diminishes their band depth. This was readily observed in this study by the common presence of zeolites in XRD and SEM, while precise identification in NIR was only achieved for NaCl experiments. This is significant as it might point to an underestimation of zeolite detections on Mars and thus have consequences for interpreting the fluid composition during martian alteration.

NIR detection of clay minerals from orbit around Mars has required the presence of >20% clay minerals (Poulet et al. 2008). A possible way to increase the detection performance of the NIR observations could be to increase spatial resolution. Such improvements of the detection performance have already been reported for orbital observations of Mars (Carter et al. 2015) and a new generation of microscopic imaging NIR spectrometer is currently awaiting deployment (Pilorget and Bibring 2013; Riu et al. 2018), allowing microscopic NIR observations of any rock sample at a scale down to 20 µm. Such instrumentation will clearly increase the capability to detect minor phases with the additional advantage of being able to map their detailed distribution.

Some discrepancies are seen between NIR and XRD/SEM-EDS analysis during detailed comparison of minor chlorite phases: 1) The NIR reflectance spectra suggest the presence of the trioctahedral chlorite due to the a 2.34 µm absorption band (Bishop et al. 2008) after 32 days experimental run time (Va, Fig. 2B) which was not observed by XRD. 2) Chlorite/smectite was only detected by XRD and/or SEM at elevated temperature after 21 days experimental run time, independent of content of dissolved CO_2 or whether rock- or fluid-dominated. 3) More challenging is the discrimination of dioctahedral and trioctahedral phyllosilicates between the methods. Only the latter variety was identified by XRD, while NIR detects dioctahedral and trioctahedral smectites and/or chlorites. A similar observation was inferred by Viennet et al. (2017), and it may indicate that NIR is more sensitive for discriminating such minerals.

In pure water experiments unambiguous detection of zeolites was only possible by XRD and/or SEM analysis, with Ca-zeolite the most abundant species and a minor Na-zeolite (analcime) also present (Table 4). Weak signatures that might be attributed to zeolites were however observed in the 2.5–3.2 µm region of the NIR reflectance spectra.

Controls on secondary alteration phases

The secondary minerals under rock-dominated conditions (Table 4) formed by condensation of liquid water on the micronized basalt allowing aqueous mineral dissolution-precipitation processes at very low water:rock ratios (Yeşilbaş and Boily 2016). The observed mineralogy in rock- and fluid-dominated conditions was comparable. This shows that a high W:R ratio is not required for the formation of secondary phases. Moreover, the W:R ratio does not change the alteration mineralogy. But the degree of alteration was generally more advanced in the fluid-dominated compared to the rock-dominated samples. This is reflected in the amorphous component and appearance of mineral peaks in XRD diffractograms. Further support is seen in NIR analyses where the fluid-dominated experiments consistently produced the deepest absorption bands.

Based on corresponding observations of XRD signals and in SEM studies, increased temperature (200°C) and/or elevated content of dissolved CO_2 resulted in faster basalt alteration. This is further supported by the increase in reaction water Cl from 120°C to 200°C with the highest concentration with 1 bar CO_2 saturation (Table 5). This assumes that Cl is a conservative element and not incorporated in any secondary phases. The increased reactivity is likely a result of the initial increased acidity caused by CO_2 dissolution, allowing more basalt to dissolve before pH is buffered to higher values (Table 6). Measured pH at end of experiments for atmospheric CO_2 saturation indicate dissolution of ~19% and ~38% of the basalt at 120°C and 200°C, respectively (Fig. 6E). Increased basalt reactivity in the rock-dominated system due to increased temperature and CO_2 content are in line with previous studies (Loring et al. 2011; Schaef et al. 2011). It should be noted that a comparison between modelled and measured pH for the CO_2 charged experiment at 200°C indicates very little basalt dissolution (Fig. 6E). The low pH in the experiment suggests that too much calcite precipitated in the model, allowing consumption of CO_2 and larger increase in pH. Calcite precipitation may have been reduced because of competition from other Ca-bearing minerals (e.g., zeolites), or because of the large Ca^{2+}/CO_3^{2-} ratio in solution (Hellevang et al. 2016).

Introduction of a saline fluid also seems to increase the rate of glass dissolution. This was observed in XRD diffractograms where the pattern contribution of the glass was reduced using saline fluids compared to the reference experiment using deionised water. These observations are additionally supported by NIR analyses, where the most prominent absorption features were observed in experiments using saline fluids. This is in agreement with previous studies where basaltic glass dissolution rates increase with ionic strength (Wolff-Boenisch et al. 2011; Morin et al. 2015).

Formation of calcite under rock-dominated conditions was observed in CO_2 charged experiments regardless of temperature and at 200°C for atmospheric CO_2 saturation (Table 4). For the atmospheric CO_2 saturated experiments it is suggested that the increased temperature resulted in higher basalt reactivity with carbon sourced from the basalt (Table 1). These observations suggest that increased content of dissolved CO_2 in the vapor, highest with 1 bar CO_2 saturation (Table 6), promotes carbonate formation. Previously performed experiments (Schaef et al. 2011; Miller et al. 2013) have shown increased carbonation of wollastonite along with higher basalt reactivity at elevated temperatures and pressures, in agreement with our results.

The observed saponite most likely formed by heterogeneous nucleation (Nagy et al. 1999), based on the apparent saponite coatings on basalt (Figs. 4A, B and C). Additionally, it was probably the first alteration mineral to form in abundances detectable by XRD and NIR. This is reflected in the scarcity of other secondary phases in the low temperature experiments (Ia, Ib, and IIb, Table 4). Chloritization of saponite occurred at elevated temperature (200°C), indicated by the XRD presence of chlorite/smectite (Table 4). Clinochlore was predicted to form in all the modeled scenarios except the 120°C and 1 bar initial pCO_2 (Fig. 6). The mixed-phase chlorite/smectite was not incorporated in the modeled database and therefore not

allowed to precipitate. In natural settings chlorites have been found to be more stable than smectite at temperatures above ~80°C (Beaufort et al. 2015; Chang et al. 1986). Additionally, calculations of mineral saturation indices based on the reacted aqueous solutions suggest that clinochlore was supersaturated at the end of experiment (Table 5). The lack of abundant discrete chlorite in the experiments reflects the short experiment period and only partial recrystallization of the smectite into chlorite.

Zeolite formation (Table 4, Fig. 6) was to be expected in the neutral to alkaline modeled pH settings of all scenarios (Fig. 6E) (Chipera and Apps 2001; Neuhoff et al. 1999; Gysi and Stefánsson 2011). The composition of the original basalt and the subsequent formation-water chemistry likely had major influence on the species of zeolites formed, as demonstrated in previous studies (Boles 1971; Hay 1978; Höller and Wirsching 1978). This is expressed here by formation of only analcime (Na-zeolite) in saline experiments at concentrations of 1 M NaCl or higher, compared to Ca-zeolite and a minor Na-zeolite in pure water experiments, and phillipsite in the saline reference study (experiments VI, Table 4). The identified zeolites in the pure water systems are fairly in line with calculated saturation indices (SI) (Table 5). These calculations shows that several zeolites were stable at end of experiment: Na-zeolite (analcime), Ca-zeolite (scolecite) and a Ca-Na zeolite (mordenite).The reaction path model for the pure water system was in fair agreement with the experiments, demonstrating formation of one zeolite (Ca-zeolite, scolecite) independent of model setup of pure water systems (Fig. 6). The PHREEQC v3 database used cannot accurately model NaCl-dominated solutions due to limitations in the thermodynamic activity model for dissolved ions. This may be the reason for the missing Na-zeolite in the modeled scenarios.

A reduced precipitation of calcite is indicated at an elevated temperature of 200°C. This is supported by weaker carbonate absorption bands at 200°C compared to 120°C and euhedral Ca-zeolites overgrowing calcite with irregular surfaces (Fig. 4E). In contrast, it seems that the Ca-zeolite continued to grow throughout the duration of the experiment. Hellevang et al. (2016) showed that a combination of slow carbonate precipitation rates at acidic conditions and smectite coatings may inhibit precipitation of carbonates. Additionally, competing reactions for divalent cations between carbonates and secondary silicates (phyllosilicates and zeolites) have shown to limit the potential for carbonate formation (Gysi and Stefánsson 2011; Aradóttir et al. 2012). The results from this study support these observations where formation of Ca-zeolites inhibits the precipitation of calcite by limiting the availability of Ca, whereas Fe and Mg are incorporated in smectites. In contrast, the reaction path model suggests competing reactions for elements between scolecite ($CaAl_2Si_3O_{10}{:}3H_2O$) and clinochlore ($Mg_5Al_2Si_3O_{10}(OH)_8$), seen by reduced formation of scolecite when clinochlore precipitates (Fig. 6). Such a competition would leave Ca available for other minerals.

Calcite was observed in all the experiments except at atmospheric CO_2 saturation and 120°C (Table 4). The CO_2 content in experiments with atmospheric CO_2 saturation was not high enough to explain the observed calcite, but additional initial carbon from the basaltic glass could have made the difference. Reaction path modeling confirmed formation of calcite in all the modeled scenarios (Fig. 6). This illustrates that the initial basaltic carbon content (Table 1) was sufficient for carbonate mineral precipitation, with the largest predicted amounts in the CO_2 charged scenarios (Fig. 6). Gysi and Stefánson (2012a) observed a change from Ca-Mg-Fe carbonates + chalcedony at 75°C to Mg-Fe phyllosilicates + calcite at 150°C and higher, using elevated pCO_2 (10–25 bar). In the current experiments calcite is the dominant carbonate species (Table 4) and Mg and Fe where incorporated in saponite and also chlorite/smectite at elevated temperatures, in agreement with the reaction path model where calcite, Mg-saponite, and Mg-nontronite formed in all the modeled scenarios. Moreover, calculations of saturation indices support this where calcite is stable mineral, and dolomite

and siderite being undersaturated (Table 5). This supports the observations of Gysi and Stefánsson (2012a) where a change in carbonate mineral species formation could occur below 120°C.

Martian implications

The NIR investigations performed by the orbiters Mars Express and Mars Reconnaissance Orbiter (MRO) have revolutionized our understanding of the alteration development that occurred on the surface of Mars (e.g. Bibring et al. 2005; Poulet et al. 2005; Bibring et al. 2006; Mustard et al. 2008). In this framework, the alteration materials produced in our experiments were analyzed with multiple techniques including NIR characterization so that the results can also be useful for interpreting the past orbital observations and future measurements performed by the planned *in situ* missions Mars2020 and ExoMars, whose payloads include NIR spectrometers for the first time in the space exploration of Mars (Pilorget and Bibring 2013).

This study demonstrates that minerals (saponite, chlorite/smectite and Ca-/Na-zeolites) comparable to those observed on Mars can be formed in hydrothermal alteration experiments with an analog basaltic glass under a variety of water:rock ratios, temperatures, dissolved CO_2, and salt (NaCl) concentrations.

Detection of glass in orbital spectra is difficult due to their broad and shallow absorption features, conclusive identification of glass in martian impact material or within basalts is therefore scarce. But a few occurrences have been observed in impact deposits, pyroclastic material and in volcanic derived sediments (Horgan and Bell 2012: Cannon and Mustard 2015; Cannon et al. 2017a). Occasionally the glass components occur together with mafic minerals showing that mixtures of glass and crystalline basalts do occur (Cannon and Mustard 2015; Cannon et al. 2017a), with possible silica leach-rinds attesting alteration under water confined conditions (Horgan and Bell 2012). The experimental material used here is not a pure glass phase, but contain a small portion of forsterite (Table 4). Experiments performed in closed systems should form the same authigenic phases from crystalline and vitric basalts, and their combination (e.g. Hawkins and Rustum 1963; Seyfried and Bischoff 1979; Gislason et al. 1993). This is also inferred by formation of phyllosilicates in the Gale crater where essential elements were sourced from olivine and a glass phases resulting in a phyllosilicate of similar composition as observed in the current experiment (Bridges et al. 2015). But, due to differences in dissolution rates of crystalline phases and glass the rate of formation may not be comparable (Gudbrandsson et al. 2011). Additionally, martian hydrous alteration occurring in open systems might not result in a mineral assemblage similar to observed here, but give Al-rich clays as postulated for surface weathered clays (Ehlmann et al. 2011b). The reason for this is that transport of elements ensures formation water concentration of Fe and Mg below equilibrium saturation with respect to Fe/Mg-smectites. But, due to the low solubility of aluminum, Al-rich phases such as kaolin precipitate. Based on the current experiments it is not possible to distinguish between closed system alteration caused by endo- or exogenic environments. Both environments have been proposed for Mars, where the former probably has been important in large-scale-tectono-magmatic complexes such as Tharsis and Elysium (Schulze-Makuch et al. 2007).

Cannon et al. (2017b) performed basalt alteration experiments using steam or a supercritical H_2O atmosphere in combination with and without CO_2 gas. This was done to explore formation of primordial clays; the interaction between the basaltic crust and a dense steam or supercritical atmosphere outgassed during magma ocean cooling. The authigenic phases produced in those experiments resembles the results obtained in the current experiment at low W:R (condensed water vapor). The temperatures used in the Cannon et al. (2017b)

experiments are higher (325 - 425°C) compared to the current experiment, and expands the conditions to a lower H_2O vapor activity where clay minerals can form.

Phyllosilicates (saponite and chlorite/smectite) and zeolites formed as the most abundant mineral groups in both rock- and fluid-dominated experiments (Table 4). These minerals may therefore form under conditions where water vapor was present; for example as steam propagates from a heated water table e.g., produced by an impact event (Newsom 1980). The rising steam would condense as liquid water on the rock as it propagates upwards. Vent features are observed in martian craters (Tornabene et al. 2009; Fairén et al. 2010; Marzo et al. 2010) and terrestrial (Osinski et al. 2001), attesting that migration of subsurface sourced water/steam has occurred. Modelled martian impact-induced hydrothermal systems produce circulating fluids and steams at temperatures within the experimental range employed here (Rathbun and Squyres 2002; Abramov and Kring 2005; Schwenzer and Kring 2009). The minerals produced in the laboratory experiments and observed in martian craters are indications that impact-induced hydrothermal alteration may have occurred, and that not all impact-related phyllosilicates were formed prior to and excavated by the impact event (see e.g. Fairén et al. 2010).

Zeolites (Na-zeolite, analcime) have been observed on Mars in a few occurrences, primarily related to impact crater settings (Ehlmann et al. 2009; Carter et al. 2013; Carrozzo et al. 2017). Ehlmann et al. (2011a) described martian zeolite exposures in combination with silica, Fe/Mg-smectite (e.g., nontronite and saponite) and chlorite and related this to alteration by hydrothermal fluids or low grade metamorphism. Our experiments reproduce a similar suite of minerals: saponite, chlorite/smectite, Ca- and minor Na-zeolites. In the saline (NaCl) experiments only the sodium zeolite variant was observed, related to excess of Na. The discrepancy of zeolite detections between XRD/SEM-EDS and NIR in the current experiments might indicate that the abundance of zeolites has been under-reported in martian NIR studies. Recent advances in NIR analytical methods should further increase the detections on Mars and provide a better understanding of processes related to martian impacts and secondary alterations. This is important as identification of zeolite phases may permit inference of the variations of the fluid composition during alteration, where various zeolite species reflect different aqueous compositions.

Calcite is not commonly observed on Mars, but magnesium carbonates are present (Ehlmann et al. 2008; Ehlmann et al. 2009; Carter et al. 2013). As discussed above the current experiments indicate that the change from Fe-Mg-carbonates to calcite could occur below 120°C as calcite is the only observed carbonate in the current experiment. According to our experiments and reaction path model, we would expect abundant carbonate formation if the martian atmosphere had elevated CO_2 pressures or contained dissolved basaltic carbon. Additionally, the modeled pH suggests no pH effect on precipitated carbonate species at pH >6 (Fig. 6). If the modeled scenarios are valid for martian hydrous alteration settings, calcite is expected to form at pH above 6. The lack of widespread martian carbonate deposits may however be explained by: 1) acid waters that have dissolved earlier formed carbonates, or prevented carbonates to grow in the first place (Fairén et al. 2004); 2) deep crustal sequestration (Edwards and Ehlmann 2015); or 3) too low partial pCO_2 pressures (Bristow et al. 2017).

Schieber et al. (2017) suggested that at least some of the clay minerals in the Gale crater had a detrital origin. This was based on the high abundance of amorphous material, variable clay mineral composition and bulk rock chemistry in the samples. As described earlier in this study, chlorite/smectite was observed in the experiment together with saponite, possibly indicating chloritization of saponite, supported by the reaction path model with co-precipitation of phyllosilicates (Mg-saponite and Mg-nontronite) and clinochlore. The maximum burial temperature in the Gale crater has been estimated to 75°C (Hahn et al. 2011),

slightly above the temperature where chloritization of saponite can occur in terrestrial diagenetic settings (Beaufort et al. 2015; Dypvik 1983). This suggests that *in situ* chloritization is a possible explanation of the observed chloritized saponite in the Gale crater.

Martian subsurface hydrous alteration probably occurred under anoxic conditions with the formation of ferrous smectites and possibly aluminous silicate minerals, assuming negligible atmospheric interaction and low sulfur content (Ehmann et al. 2011b; Catalano 2013; Osinski et al. 2013). This matches well the current experiments where trioctahedral saponite precipitated along with zeolites. Additionally, previous analysis show that the Stapafell basalt mainly contain Fe^{2+} (Oelkers and Gislason 2001), and combined with the initial experimental conditions and secondary phases formed the experiments most likely progressed without significant Fe^{2+} oxidation. Strongly reducing conditions in terrestrial hydrothermal systems has been postulated as a source for hydrogen production observed in the Yellowstone National Park and in the Columbia River Basalt (Stevens and McKinley 1995, 2000; Spear et al. 2005). Studies by Catalano et al. (2013) and Chemtob et al. (2017) suggest that the low abundance of ferrous phyllosilicates might be a result of post-formational oxidation with formation of ferric smectites, rather than original formation in an oxidizing environment. Moreover, Catalano et al. (2013) suggest that the scarce Al-silicate identifications on Mars might indicate that subsurface alteration at elevated temperature is an unlikely scenario. The current experiments agree on formation of trioctahedral smectites and aluminosilicates, but they also show that identification of zeolites are difficult using NIR and the confined identification on Mars might be a result of the difficulties in identifying the mineral species and not that they are not present.

CONCLUSION

The performed experiments show that a similar suite of minerals as observed on Mars can be formed by hydrothermal alteration of a basaltic glass. Saponite, the most abundant phyllosilicate, is observed in XRD, NIR and SEM analysis, regardless of water:rock ratio, temperature, CO_2 saturation, and water chemistry. This is further supported by reaction path modeling where phyllosilicates (Mg-saponite, Mg-nontronite, and clinochlore) are commonly the largest mineral group. These observations suggest that a similar suite of minerals will form in both rock- and fluid-dominated settings under martian-like alteration settings. The experiments and geochemical modeling show that fluid composition controls the zeolite species forming. Moreover, martian secondary minerals associated with martian impact craters can be formed by circulating fluids and by evaporating vapors. Alteration by water vapor has been previously proposed and the current study expands the conditions to a lower H_2O vapor activity than previously suggested. Finally, the discrepancy between identification and discrimination of zeolites between XRD/SEM-EDS and NIR suggests that zeolites might be underestimated in martian studies. The combined analysis of common martian alteration products by XRD, SEM and NIR could be useful in interpreting past orbital NIR analyses and the coming *in situ* NIR analyses on Mars. In particular, better characterizations of zeolites should yield more information on the fluid chemistry during alteration.

Acknowledgements – We thank Berit Løken Berg and Muriel Marie Laure Erambert for technical assistance in the SEM measurements, Ray Ferrell Jr. and Maarten Aerts for support in the XRD interpretations, Adrian Read for proof reading and Sigurdur Gislason for supplying us with the volcanic glass used in the experiments. Additionally, we thank Alberto G. Fairén and an anonymous reviewer for their thorough and constructive comments, and G. Osinski for handling of the manuscript. The authors acknowledge the support of the Research Council of Norway (NFR) through the Centre of Excellence funding scheme, project number

223272 (CEED). The research leading to these results has received funding from the European Union's Horizon 2020 Research and Innovation Programme, under Grant Agreement no 687302. The paper is a result of the bilateral collaboration project *Earth-Mars Analogues: Origination and Distribution of Clay Minerals in Impact Crater Environments* with the NFR contribution (244111/O30) and the French contribution Aurora PHC 34016SG.

REFERENCES

Abramov O., and Kring D. A. 2005. Impact-induced hydrothermal activity on early Mars. *Journal of Geophysical Research: Planets (1991–2012)* 110:E12S09. https://doi.org/10.1029/2005JE002453

Aradóttir E. S. P., Sonnenthal E. L., Björnsson G., and Jónsson H. 2012. Multidimensional reactive transport modeling of CO_2 mineral sequestration in basalts at the Hellisheidi geothermal field, Iceland. *International Journal of Greenhouse Gas Control* 9:24–40. https://doi.org/10.1016/j.ijggc.2012.02.006

Beaufort D., Rigault C., Billon S., Billault V., Inoue A., Inoue S., and Patrier P. 2015. Chlorite and chloritization processes through mixed-layer mineral series in low-temperature geological systems–a review. *Clay Minerals* 50:497–523. https://doi.org/10.1180/claymin.2015.050.4.06

Bibring J. -P., Soufflot A., Berthé M., Langevin Y., Gondet B., Drossart P., Bouyé M., Combes M., Puget P., Semery A., Bellucci G., Formisano V., Moroz V., Kottsov V., Bonello G., Erard S., Forni O., Gendrin A., Manaud N., Poulet F., Poulleau G., Encrenaz T., Fouchet T., Melchiori R., Altieri F., Ignatiev N., Titov D., Zasova L., Coradini A., Capacionni F., Cerroni P., Fonti S., Mangold N., Pinet P., Schmitt B., Sotin C., Hauber E., Hoffmann H., Jaumann R., Keller U., Arvidson R., Mustard J., and Forget F. 2004. OMEGA: Observatoire pour la Minéralogie, l'Eau, les Glaces et l'Activité. In Mars Express: *The scientific payload*, edited by Wilson A. and Chicarro A. Noordwijk, the Netherlands: European Space Agency Special Publication. pp. 37–49.

Bibring J. -P., Langevin Y., Gendrin A., Gondet B., Poulet F., Berthé M., Soufflot A., Arvidson R., Mangold N., and Mustard J. 2005. Mars surface diversity as revealed by the OMEGA/Mars Express observations. *Scienc*e 307:1576–1581. https://doi.org/10.1126/science.1108806

Bibring J. -P., Langevin Y., Mustard J. F., Poulet F., Arvidson R., Gendrin A., Gondet B., Mangold N., Pinet P., and Forget F. 2006. Global mineralogical and aqueous Mars history derived from OMEGA/Mars Express data. *Science* 312:400–404. https://doi.org/10.1126/science.1122659

Bishop J. L., Lane M. D., Dyar M. D., and Brown A. J. 2008. Reflectance and emission spectroscopy study of four groups of phyllosilicates: smectite, kaolinite-serpentines, chlorites and micas. *Clay minerals* 43:35–54. https://doi.org/10.1180/claymin.2008.043.1.03

Boles J. R. 1971. Synthesis of analcime from natural heulandite and clinoptilolite. *American Mineralogist* 56:1724.

Bridges J. C., Schwenzer S. P., Leveille R., Westall F., Wiens R. C., Mangold N., Bristow T., Edwards P., and Berger G. 2015. Diagenesis and Clay mineral formation at Gale Crater, Mars. *Journal of Geophysical Research: Planets* 120:1–19. https://doi.org/10.1002/2014JE004757

Bristow T. F., Bish D. L., Vaniman D. T., Morris R. V., Blake D. F., Grotzinger J. P., Rampe E. B., Crisp J. A., Achilles C. N., Ming D. W., Ehlmann B. L., King P. L., Bridges J C., Eigenbrode J. L., Sumner D. Y., Chipera S. J., Moorokian J. M., Treiman A. H., Morrison S. M., Downs R. T., Farmer J. D., Marais D. D., Sarrazin P., Floyd M. M., Mischna M. A., and McAdam A. C. 2015. The origin and implications of clay minerals from Yellowknife Bay, Gale crater, Mars. *American Mineralogist* 100:824–836. https://doi.org/10.2138/am-2015-5077CCBYNCND

Bristow T. F., Haberle R. M., Blake D. F., Des Marais D. J., Eigenbrode J. L., Fairén A. G., Grotzinger J. P., Stack K. M., Mischna M. A., Rampe E. B., Siebach K. L., Sutter B.,

Vaniman D. T., and Vasavada A. R. 2017. Low Hesperian pCO_2 constrained from in situ mineralogical analysis at Gale Crater, Mars. *Proceedings of the National Academy of Sciences of the United States of America* 114:2166–2170. https://doi.org/10.1073/pnas.1616649114

Cannon K. M., and Mustard J. F. 2015. Preserved glass-rich impactites on Mars. *Geological Society of America* 43:635–638.

Cannon K. M., Mustard J. F., Parman S. W., Sklute E. C., Dyar M. D., and Cooper R. F. 2017a. Spectral properties of Martian and other planetary glasses and their detection in remotely sensed data. *Journal of Geophysical Research: Planets 122:249–268.* https://doi.org/10.1002/2016JE005219

Cannon K. M., Parman S. W., and Mustard J. F. 2017b. Primordial clays on Mars formed beneath a steam or supercritical atmosphere. *Nature* 552:88–91. https://doi.org/10.1038/nature24657

Carrozzo F. G., Di Achille G., Salese F., Altieri F., and Bellucci G. 2017. Geology and mineralogy of the Auki Crater, Tyrrhena Terra, Mars: A possible post impact-induced hydrothermal system. *Icarus* 281:228–239. https://doi.org/10.1016/j.icarus.2016.09.001

Carter J., Loizeau D., Mangold N., Poulet F., and Bibring J. -P. 2015. Widespread surface weathering on early Mars: A case for a warmer and wetter climate. *Icarus* 248:373–382. https://doi.org/10.1016/j.icarus.2014.11.011

Carter J., Poulet F., Bibring J. -P., Mangold N., and Murchie S. 2013. Hydrous minerals on Mars as seen by the CRISM and OMEGA imaging spectrometers: Updated global view. *Journal of Geophysical Research: Planets* 118:831–858. https://doi.org/10.1029/2012JE004145

Catalano J. G. 2013. Thermodynamic and mass balance constraints on iron-bearing phyllosilicate formation and alteration pathways on early Mars. *Journal of Geophysical Research: Planets* 118:2124–2136. https://doi.org/10.1002/jgre.20161

Chang H. K., Mackenzie F. T., and Schoonmaker J. 1986. Comparisons between the diagenesis of dioctahedral and trioctahedral smectite, Brazilian offshore basins. *Clays and Clay minerals* 4:407–423.

Chemtob S. M., Nickerson R. D., Morris R. V., Agresti D. G., and Catalano J. G. 2017. Oxidative alteration of ferrous smectites and implications for the redox evolution of early Mars. *Journal of Geophysical Research: Planets* 122:2469–2488. https://doi.org/10.1002/2017JE005331

Chipera S. J., and Apps J. A. 2001. Geochemical stability of natural zeolites. *Reviews in mineralogy and geochemistry* 45:117–161.

Clark B. C., and Van Hart D. C. 1981. The salts of Mars. *Icarus* 45:370–378. https://doi.org/10.1016/0019-1035(81)90041-5

Dehouck E., Mangold N., Le Mouélic S., Ansan V., and Poulet F. 2010. Ismenius Cavus, Mars: A deep paleolake with phyllosilicate deposits. *Planetary and Space Science* 58:941–946. https://doi.org/10.1016/j.pss.2010.02.005

Doebelin N., and Kleeberg R. 2015. Profex: a graphical user interface for the Rietveld refinement program BGMN. *Journal of applied crystallography* 48:1573–1580. https://doi.org/10.1107/S1600576715014685

Dypvik H. 1983. Clay mineral transformations in Tertiary and Mesozoic sediments from North Sea. *AAPG Bulletin* 67:160–165.

Edwards C. S., and Ehlmann B. L. 2015. Carbon sequestration on Mars. *Geology* 43:863–866. https://doi.org/10.1130/G36983.1

Ehlmann B. L., Mustard J. F., Clark R. N., Swayze G. A., and Murchie S. L. 2011a. Evidence for low-grade metamorphism, hydrothermal alteration, and diagenesis on Mars from

phyllosilicate mineral assemblages. *Clays and Clay Minerals* 59:359–377. https://doi.org/10.1346/CCMN.2011.0590402

Ehlmann B. L., Mustard J. F., Murchie S. L., Bibring J. -P., Meunier A., Fraeman A. A., and Langevin Y. 2011b. Subsurface water and clay mineral formation during the early history of Mars. *Nature* 479:53–60. https://doi.org/10.1038/nature10582

Ehlmann B. L., Mustard J. F., Swayze G. A., Clark R. N., Bishop J. L., Poulet F., Des Marais D. J., Roach L. H., Milliken R. E., Wray J. J., Barnouin-Jha O., and Murchie S. L. 2009. Identification of hydrated silicate minerals on Mars using MRO-CRISM: Geologic context near Nili Fossae and implications for aqueous alteration. *Journal of Geophysical Research: Planets* 114. https://doi.org/10.1029/2009JE003339

Ehlmann B. L., Mustard J. F., Murchie S. L., Poulet F., Bishop J. L., Brown A. J., Calvin W. M., Clark R. N., Des Marais D. J., Milliken R. E., Roach L. H., Roush T. L., Swayze G. A., and Wray J. J. 2008. Orbital identification of carbonate-bearing rocks on Mars. *Science* 322:1828–1832. https//doi.org/10.1126/science.1164759

Fairén A. G., Fernández-Remola D., Dohm J. M., Baker V. R., and Amils R. 2004. Inhibition of carbonate synthesis in acidic oceans on early Mars. *Nature* 431:423–426

Fairén A. G., Davila A. F., Gago-Duport L., Amils R., and McKay, C. P. 2009. Stability against freezing of aqueous solutions on early Mars. *Nature* 459:401–404. https://doi.org/10.1038/nature07978

Fairén A. G., Chevrier V., Abramov O., Marzo G. A., Gavin P., Davila A. F., Tornabene L. L., Bishop J. L., Roush T. L., Gross C., Kneissl T., Uceda E. R., Dohm J. M. Sculze-Makuch D., Rodrígues-Aguilar J. A., Amils R., and McKay C. P. 2010. Noachian and more recent phyllosilicates in impact craters on Mars. *Proceedings of the National Academy of Sciences of the United States of America* 107:12095–12100. https://doi.org/10.1073/pnas.1002889107

Forget F., Wordsworth R., Millour E., Madeleine J. -B., Kerber L., Leconte J., Marcq E., and Haberle R. M. 2013. 3D modelling of the early martian climate under a denser CO_2 atmosphere: Temperatures and CO_2 ice clouds. *Icarus* 222:81–99. https://doi.org/10.1016/j.icarus.2012.10.019

Galeczka I., Wolff-Boenisch D., Oelkers E. H., and Gislason S. R. 2014. An experimental study of basaltic glass–H_2O–CO_2 interaction at 22 and 50°C: Implications for subsurface storage of CO_2. *Geochimica et Cosmochimica Acta* 126:123–145. https://doi.org/10.1016/j.gca.2013.10.044

Gaudin A., Dehouck E., Grauby O., and Mangold N. 2018. Formation of clay minerals on Mars: Insights from long-term experimental weathering of olivine. *Icarus* 311:210–223. https://doi.org/10.1016/j.icarus.2018.01.029

Gislason S. R., Veblen D. R., and Livi K. J. T. 1993. Experimental meteoric water-basalt interactions: Characterization and interpretation of alteration products. *Geochimica et Cosmochimica Acta* 57:1459–1471. https://doi.org/10.1016/0016-7037(93)90006-I

Goldberg D. S., Takahashi T., and Slagle A. L. 2008. Carbon dioxide sequestration in deep-sea basalt. *Proceedings of the National Academy of Sciences of the United States of America* 105:9920–9925. https://doi.org/10.1073/pnas.0804397105

Grindrod P. M., West M., Warner N. H., and Gupta S. 2012. Formation of an Hesperian-aged sedimentary basin containing phyllosilicates in Corporates Catene, Mars. *Icarus* 218:178–195. https://doi.org/10.1016/j.icarus.2011.11.027

Gudbrandsson S., Wolff-Boenisch D., Gislason S. R., and Oelkers E. H. 2011. An experimental study of crystalline basalt dissolution from $2 \leqslant pH \leqslant 11$ and temperatures from 5 to 75°C. *Geochimica et Cosmochimica Acta* 75.19:5496–5509. https://doi.org/10.1016/j.gca.2011.06.035

Gysi A. P., and Stefánsson A. 2011. CO_2–water–basalt interaction. Numerical simulation of low temperature CO_2 sequestration into basalts. *Geochimica et Cosmochimica Acta* 75:4728–4751. https://doi.org/10.1016/j.gca.2011.05.037

Gysi A. P., and Stefánsson A. 2012a. Experiments and geochemical modeling of CO_2 sequestration during hydrothermal basalt alteration. *Chemical Geology* 306:10–28. https://doi.org/10.1016/j.chemgeo.2012.02.016

Gysi A. P., and Stefánsson A. 2012b. Mineralogical aspects of CO_2 sequestration during hydrothermal basalt alteration — An experimental study at 75 to 250°C and elevated pCO_2. *Chemical Geology* 306–307:146–159. https://doi.org/10.1016/j.chemgeo.2012.03.006

Hagerty J. J., and Newsom H. E. 2003. Hydrothermal alteration at the Lonar Lake impact structure, India: Implications for impact cratering on Mars. *Meteoritics & Planetary Science* 38:365–381. https://doi.org/10.1111/j.1945-5100.2003.tb00272.x

Hahn B., McSween H., and Tosca N. 2011. Constraints on the stabilities of observed martian secondary mineral phases from geothermal gradient models (abstract). *Lunar and Planetary Science Conference*, p. 2340.

Hawkins D. B., and Rustum R. 1963. Experimental hydrothermal studies on rock alteration and clay mineral formation. *Geochimica et Cosmochimica Acta* 27:1047–1054. https://doi.org/10.1016/0016-7037(63)90065-6

Hay R. L. 1978. Geologic occurrence of zeolites. *Natural zeolites: occurrence, properties, use*, edited by Sand L. S. and Mumptom F. A. Pergamon Press, pp. 135–143.

Helgeson H. C. 1968. Evaluation of irreversible reactions in geochemical processes involving minerals and aqueous solutions—I. Thermodynamic relations. *Geochimica et Cosmochimica Acta* 32:853–877. https://doi.org/10.1016/0016-7037(68)90100-2

Hellevang H., Dypvik H., Kalleson E., Pittarello L., and Koeberl C. 2013. Can alteration experiments on impact melts from El'gygytgyn and volcanic glasses shed new light on the formation of the Martian surface? *Meteoritics & Planetary Science* 48:1287–1295. https://doi.org/10.1111/maps.12046

Hellevang H., Haile B. G., and Tetteh A. 2016. Experimental study to better understand factors affecting the CO_2 mineral trapping potential of basalt. *Greenhouse Gases: Science and Technology* 7:143–157. https://doi.org/10.1002/ghg.1619

Horgan B., and Bell III J. F. 2012. Widespread weathered glass on the surface of Mars. *Geological Society of America* 40:391–394. https://doi.org/10.1130/G32755.1

Höller H., and Wirsching U. 1978. Experiments on the formation of zeolites by hydrothermal alteration of volcanic glasses. *Natural zeolites: occurrence, properties, use*, edited by Sand L. S. and Mumptom F. A. Pergamon Press, pp. 329–336.

Jouglet D., Poulet F., Milliken R., Mustard J., Bibring J. -P., Langevin Y., Gondet B., and Gomez C. 2007. Hydration state of the Martian surface as seen by Mars Express OMEGA: 1. Analysis of the 3 μm hydration feature. *Journal of Geophysical Research: Planets* 112. https://doi.org/10.1029/2006JE002846

Le Deit L., Flahaut J., Quantin C., Hauber E., Mège D., Bourgeois O., Gurgurewicz J., Massé M., and Jaumann R. 2012. Extensive surface pedogenic alteration of the Martian Noachian crust suggested by plateau phyllosilicates around Valles Marineris. *Journal of Geophysical Research: Planets* 117. https://doi.org/10.1029/2011JE003983

Loring J. S., Thompson C. J., Wang Z., Joly A. G., Sklarew D. S., Schaef H. T., Ilton E. S., Rosso K. M., and Felmy A. R. 2011. In situ infrared spectroscopic study of forsterite

carbonation in wet supercritical CO_2. *Environmental science & technology* 45:6204–6210. https://doi.org/10.1021/es201284e

Mangold N., Carter J., Poulet F., Dehouck E., Ansan V., and Loizeau D. 2012. Late Hesperian aqueous alteration at Majuro crater, Mars. *Planetary and Space Science* 72:18–30. https://doi.org/10.1016/j.pss.2012.03.014

Marzo G. A., Davila A. F., Tornabene L. L., Dohm J. M., Fairén A. G., Gross C., Kneissl T., Bishop J. L., Roush T. L., and McKay C. P. 2010. Evidence for Hesperian impact-induced hydrothermalism on Mars. *Icarus* 208:667–683. https://doi.org/10.1016/j.icarus.2010.03.013

McGrail B. P., Schaef H. T., Ho A. M., Chien Y. J., Dooley J. J., and Davidson C. L. 2006. Potential for carbon dioxide sequestration in flood basalts. *Journal of Geophysical Research: Solid Earth* 111. https://doi.org/10.1029/2005JB004169

McSween H. Y., Taylor G. J., and Wyatt M. B. 2009. Elemental composition of the Martian crust. *Science* 324:736–739. https://doi.org/10.1126/science.1165871

Miller Q. R. Jr., Thompson C. J., Loring J. S., Windisch C. F., Bowden M. E., Hoyt D. W., Hu J. Z., Arey B. W., Rosso K. M., and Schaef H. T. 2013. Insights into silicate carbonation processes in water-bearing supercritical CO_2 fluids. *International journal of greenhouse Gas Control* 15:104–118. https://doi.org/10.1016/j.ijggc.2013.02.005

Moore D., and Reynolds R. 1997. X-ray diffraction and the identification and analysis of clay minerals, 2nd edition, Oxford, Oxford University press 378 p.

Morin G. P., Vigier N., and Verney-Carron A. 2015. Enhanced dissolution of basaltic glass in brackish waters: Impact on biogeochemical cycles. *Earth and Planetary Science Letters* 417:1–8. https://doi.org/10.1016/j.epsl.2015.02.005

Murchie S. L., Arvidson R., Bedini P., Beisser K., Bibring J. -P., Bishop J., Boldt J., Cavender P., Choo T., Clancy R. T., Darlington E. H., Des Marais D., Espiritu R., Fort D., Green R., Guinness E., Hayes J., Hash C., Heffernan K., Hemmler J., Heyler G., Humm D., Hutcheson J., Izenberg N., Lee R., Lees J., Lohr D., Malaret E., Martin T., McGovern J. A., McGuire P., Morris R., Mustard J., Pelkey S., Rhodes E., Robinson M., Roush T., Schaefer E., Seagrave G., Seelos F., Silverglate P., Slavney S., Smith M., Shyong W. J., Strohbehn K., Taylor H., Thompson P., Tossman B., Wirzburger M., and Wolff M. 2007. Compact Reconnaissance Imaging Spectrometer for Mars (CRISM) on Mars Reconnaissance Orbiter (MRO). *Journal of Geophysical Research* 112:E05S03. https://doi.org/10.1029/2006JE002682

Mustard J. F., Murchie S. L., Pelkey S. M., Ehlmann B. L., Milliken R. E., Grant J. A., Bibring J. -P., Poulet F., Bishop J., Dobrea E. N., Roach L., Seelos F., Arvidson R. E., Wiseman S., Green R., Hash C., Humm D., Malaret E., McGovern J. A., Seelos K., Clancy T., Clark R., Marais D. D., Izenberg N., Knudson A., Langevin Y., Martin T., McGuire P., Morris R., Robinson M., Roush T., Smith M., Swayze G., Taylor H., Titus T., and Wolff M. 2008. Hydrated silicate minerals on Mars observed by the Mars Reconnaissance Orbiter CRISM instrument. *Nature* 454:305–309. https://doi.org/10.1038/nature07097

Nagy K. L., Cygan R. T., Hanchar J. M., and Sturchio N. C. 1999. Gibbsite growth kinetics on gibbsite, kaolinite, and muscovite substrates: atomic force microscopy evidence for epitaxy and an assessment of reactive surface area. *Geochimica et Cosmochimica Acta* 63:2337–2351. https://doi.org/10.1016/S0016-7037(99)00118-0

Neuhoff P. S., Fridriksson T., Arnorsson S., and Bird D. K. 1999. Porosity evolution and mineral paragenesis during low-grade metamorphism of basaltic lavas at Teigarhorn, eastern Iceland. *American Journal of Science* 299.6:467–501.

Newsom H. E. 1980. Hydrothermal alteration of impact melt sheets with implications for Mars. *Icarus* 44:207–216. https://doi.org/10.1016/0019-1035(80)90066-4

Newsom H. E., Hagerty J. J., and Goff F. 1999. Mixed hydrothermal fluids and the origin of the Martian soil. *Journal of Geophysical Research: Planets* 104:8717–8728. https://doi.org/10.1029/1998JE900043

Oelkers E. H., and Gislason S. R. 2001. The mechanism, rates and consequences of basaltic glass dissolution: I. An experimental study of the dissolution rates of basaltic glass as a function of aqueous Al, Si and oxalicacid concentration at 25°C and pH = 3 and 11. *Geochimica et Cosmochimica Acta* 65:3671–3681. https://doi.org/10.1016/S0016-7037(01)00664-0

Osinski G. R. 2005. Hydrothermal activity associated with the Ries impact event, Germany. *Geofluids* 5:202–220. https://doi.org/10.1111/j.1468-8123.2005.00119.x

Osinski G. R., Spray J. G., and Lee P. 2001. Impact-induced hydrothermal activity within the Haughton impact structure, arctic Canada: Generation of a transient, warm, wet oasis. *Meteoritics & Planetary Science* 36 5:731–745. https://doi.org/10.1111/j.1945-5100.2001.tb01910.x

Osinski G. R., Tornabene L. L., Banerjee N. R., Cockell C. S., Flemming R., Izawa M. R. M., McCutcheon J., Parnell J., Preston L. J., Pickersgill A. E., Pontefract A., Sapers H. M., and Southam G. 2013. Impact-generated hydrothermal systems on Earth and Mars. *Icarus* 224:347–363. https://doi.org/10.1016/j.icarus.2012.08.030

Parkhurst D. L., and Appelo C. 2013. Description of input and examples for PHREEQC version 3: a computer program for speciation, batch-reaction, one-dimensional transport, and inverse geochemical calculations. *US Geological Survey*.

Peng D. -Y., and Robinson D. B. 1976. A new two-constant equation of state. *Industrial & Engineering Chemistry Fundamentals* 15: 59–64. https://pubs.acs.org/doi/pdf/10.1021/i160057a011

Pilorget C., and Bibring J. -P. 2013. NIR reflectance hyperspectral microscopy for planetary science: Application to the MicrOmega instrument. *Planetary and Space Science* 76:42–52. https://doi.org/10.1016/j.pss.2012.11.004

Poulet F., Bibring J. -P., Mustard J., Gendrin A., Mangold N., Langevin Y., Arvidson R., Gondet B., Gomez C., and Berthé M. 2005. Phyllosilicates on Mars and implications for early Martian climate. *Nature* 438:623–627. https://doi.org/10.1038/nature04274

Poulet F., Arvidson R., Gomez C., Morris R., Bibring J. -P., Langevin Y., Gondet B., and Griffes J. 2008. Mineralogy of Terra Meridiani and western Arabia terra from OMEGA/Mex and implications for their formation. *Icarus* 195:106–130. https://doi.org/10.1016/j.icarus.2007.11.031

Rathbun J. A., and Squyres S. W. 2002. Hydrothermal systems associated with Martian impact craters. *Icarus* 157:362–372. https://doi.org/10.1006/icar.2002.6838

Retallack G. J. 2014. Paleosols and paleoenvironments of early Mars. *Geology* 42:755–758. https://doi.org/10.1130/G35912.1

Reynolds III R., and Reynolds Jr. R. 2012. NEWMOD II a computer program for the calculation of one-dimensional diffraction patterns of mixed-layered clays.

Riu L., Bibring J. -P., Pilorget C, Poulet F., and Hamm V. 2018. The on-ground calibration performance of the hyperspectral microscope MicrOmega for the Hayabusa-2 mission. *Planetary and Space Science* 152:31–44. https://doi.org/10.1016/j.pss.2018.01.009

Schaef H. T., McGrail B. P., and Owen A. T. 2011. Basalt reactivity variability with reservoir depth in supercritical CO_2 and aqueous phases. *Energy Procedia* 4:4977–4984. https://doi.org/10.1016/j.egypro.2011.02.468

Schieber J., Bish D., Coleman M., Reed M., Hausrath E. M., Cosgrove J., Gupta S., Minitti M. E., Edgett K. S., and Malin M. 2017. Encounters with an unearthly mudstone: Understanding the first mudstone found on Mars. *Sedimentology* 64:311–358. https://doi.org/10.1111/sed.12318

Schwenzer S. P., and Kring D. A. 2009. Impact-generated hydrothermal systems capable of forming phyllosilicates on Noachian Mars. *Geology* 37:1091–1094. https://doi.org/10.1130/G30340A.1

Schwenzer S. P., Bridges J. C., Wiens R. C., Conrad P. G., Kelley S. P., Leveille R., Mangold N., Martín-Torres J., McAdam A., Newsom H., Zorzano M. P., Rapin W., Spray J., Treiman A. H., Westall F., Fairén A. G., and Meslin P. –Y. 2016. Fluids during diagenesis and sulfate vein formation in sediments at Gale crater, Mars. *Meteoritics & Planetary Science* 51:2175–2202. https://doi.org/10.1111/maps.12668

Schultz-Makuch D., Dohm J. M., Fan C., Fairén A. G., Rodriguez J. A. P., Baker V. R., and Fink W. 2007. Exploration of hydrothermal targets on Mars. *Icarus* 189:308–324. https://doi.org/10.1016/j.icarus.2007.02.007

Seyfried W. E. Jr., and Bischoff J. L. 1979. Low temperature basalt alteration by seawater: an experimental study at 70°C and 150°C. *Geochimica et Cosmochimica Acta* 43:1937–1947. https://doi.org/10.1016/0016-7037(79)90006-1

Spear J. R., Walker J. J., McCollom T. M. and Pace N. R. 2005. Hydrogen and bioenergetics in the Yellowstone geothermal ecosystem. *Proceedings of the National Academy of Sciences of the United States of America* 102:2555–2560. https://doi.org/10.1073/pnas.0409574102

Stevens T. O., and McKinley J. P. 1995. Lithoautotrophic microbial ecosystems in deep basalt aquifers. *Science* 270:103–114. https://doi.org/10.1126/science.270.5235.450

Stevens T. O., and McKinley J. P. 2000. Abiotic controls on H_2 production from basalt-water reactions and implications for aquifer biogeochemistry. *Environmental science & technology* 34:826–831. https://doi.org/10.1021/es990583g

Tornabene L., Osinski G., and McEwen A. 2009. Parautochthonous megabreccias and possible evidence of impact-induced hydrothermal alteration in Holden Crater, Mars (abstract), *Lunar and Planetary Science Conference*, p. 1766.

Vaniman D. T., Bish D. L., Ming D. W., Bristow T. F., Morris R. V., Blake D. F., Chipera S. J., Morrison S. M., Treiman A. H., Rampe E. B., Rice M., Achilles C. N., Grotzinger J. P., McLennan S. M., Williams J., Bell J. F. III, Newsom H. E., Downs R. T., Maurice S., Sarrazin P., Yen A. S., Morookian J. M., Farmer J. D., Stack K., Milliken R. E., Ehlmann B. L., Sumner D. Y., Berger G., Crisp J. A., Hurowitz J. A., Anderson R., Des Marais D. J., Stolper E. M., Edgett K. S., Gupta S., and Spanovich N. 2013. Mineralogy of a mudstone at Yellowknife Bay, Gale crater, Mars. *Science* 343:1243480. https://doi.org/10.1126/science.1243480

Viennet J. C., Bultel B., Riu L., and Werner S. C. 2017. Dioctahedral phyllosilicates versus zeolites and carbonates versus zeolites competitions as constraints to understanding early Mars alteration conditions. *Journal of Geophysical Research: Planets* 122:2328–2343. https://doi.org/10.1002/2017JE005343

Wolff-Boenisch D., Wenau S., Gislason S. R., and Oelkers E. H. 2011. Dissolution of basalts and peridotite in seawater, in the presence of ligands, and CO_2: implications for mineral sequestration of carbon dioxide. *Geochimica et Cosmochimica Acta* 75:5510–5525. https://doi.org/10.1016/j.gca.2011.07.004

Wordsworth R., Kalugina Y., Lokshtanov S., Vigasin A., Ehlmann B., Head J., Sanders C., and Wang H. 2017. Transient reducing greenhouse warming on early Mars. *Geophysical Research Letters* 44:665–671. https://doi.org/10.1002/2016GL071766

Yeşilbaş M., and Boily J. -F. 2016. Particle size controls on water adsorption and condensation regimes at mineral surfaces. *Scientific Reports* 6:32136.

Zhang F., Xu H., Konishi H., and Roden E. E. 2010. A relationship between d104 value and composition in the calcite-disordered dolomite solid-solution series. *American Mineralogist* 95:1650–1656. https://doi.org/10.2138/am.2010.3414

Table 1. Major element composition (wt%) and LOI of the Stapafell basaltic glass determined by XRF and total carbon (TC) analysis.

SiO_2	TiO_2	Al_2O_3	Fe_2O_3	MnO	MgO	CaO	Na_2O	K_2O	P_2O_5	Cr_2O_3	ZnO	SO_3	LOI	TC
47.282	1.487	14.657	12.148	0.213	10.079	11.438	1.756	0.273	0.206	0.109	0.013	0.111	-0.5	0.74

Table 2. Overview of performed experiments. L: liquid phase (w/r = 10), CV: condensed vapor phase, atm.: atmospheric CO_2 saturated, 1 bar: 1 bar CO_2 saturated.

Experiment	Temp (°C)	W:R	Init. CO_2	Type water	Run time (days)
Ia	120	L	atm.	Deionised	21
Ib	120	CV	atm.	Deionised	21
IIa	120	L	1 bar	O_2 depleted, deionised	21
IIb	120	CV	1 bar	O_2 depleted, deionised	21
IIIa	200	L	atm.	Deionised	21
IIIb	200	CV	atm.	Deionised	21
IVa	200	L	1 bar	O_2 depleted, deionised	21
IVb	200	CV	1 bar	O_2 depleted, deionised	21
Va	200	L	atm.	Deionised	32
Vb	200	CV	atm.	Deionised	32
VI-0	150	L	atm.	Deionised	42
VI-1	150	L	atm.	1 M NaCl	42
VI-2	150	L	atm.	2 M NaCl	42
VI-4	150	L	atm.	4 M NaCl	42

Table 3. Mineral species allowed forming in the reaction path model with chemical and initial basaltic glass composition.

Phases	Chemical formula
Basaltic glass	$Na_{0.072}K_{0.007}Fe_{0.193}Mg_{0.318}Al_{0.365}Ca_{0.259}P_{0.0037}SiO_{3.526}C_{0.078}$
Carbonate	
Calcite	$CaCO_3$
Dolomite	$CaMg(CO_3)_2$
Siderite	$FeCO_3$
Tectosilicate	
Quartz	SiO_2
Chalcedony	SiO_2
Zeolite	
Mesolite	$Na_{0.676}Ca_{0.657}Al_{1.99}Si_{3.01}O_{10}:2.04H_2O$
Scolecite	$CaAl_2Si_3O_{10}:3H_2O$
Mordenite	$Ca_{0.2895}Na_{0.361}Al_{0.94}Si_{5.06}O_{12}:3.468H_2O$
Analcime	$Na_{0.96}Al_{0.96}Si_{2.04}O_6:H_2O$
Phyllosilicate	
Ca-saponite	$Ca_{0.165}Mg_3Al_{0.33}Si_{3.67}O_{10}(OH)_2$
Mg-saponite	$Mg_{3.165}Al_{0.33}Si_{3.67}O_{10}(OH)_2$
Na-montmorillonite	$Na_{0.33}Mg_{0.33}Al_{1.67}Si_4O_{10}(OH)_2$
Mg-nontronite	$Mg_{0.165}Fe_2Al_{0.33}Si_{3.67}H_2O_{12}$
Ca-nontronite	$Ca_{0.165}Fe_2Al_{0.33}Si_{3.67}H_2O_{12}$
Kaolinite	$Al_2Si_2O_5(OH)_4$
Clinochlore	$Mg_5Al_2Si_3O_{10}(OH)_8$
Anhydrous Phosphates	
Hydroxyapatite	$Ca_5(PO_4)_3OH$

Table 4. Qualitative and semi-quantitative overview of minerals identified by XRD/SEM-EDS and NIR for the various experiments (Exp), divided into fluid dominated, rock dominated and saline experiments. 1–4 indicate relative abundance, 4 most and 1 least abundant. Possible identifications in brackets. MilliQ-OD: oxygen depleted MilliQ water, atm.: atmospheric CO_2 saturated, 1 bar: 1 bar CO_2 saturated, Clays: saponite and/or interstratified chlorite/smectite, Ca-z: Ca-zeolite, Na-z: Na-zeolite (analcime), Php: phillipsite, Zeo: unspecified zeolite, Sc: scolecite, Arg: aragonite, Cel: celadonite, Clc: clinochlore, Carb: unspecified carbonate. See Table 2 for experimental details.

Experimental setup					XRD/SEM-EDS								NIR				
Phase	Temp (°C)	Exp.	Init. CO_2	Clays	Ca-z	Na-z	Sc	Php	Cal	Arg	Zeo	Fo	Sap	Cel or Clc	Carb	Na-z	Zeo
Fluid dominated	120	Ia	atm.	(x)	-	-	-	-	-	-	-	2	x	-	-	-	-
		IIa	1 bar	4	2	1	-	-	1	-	-	1	x	-	x	-	x
	200	IIIa	atm.	4	3	1	-	-	1	-	-	1	x	-	x	-	x
		IVa	1 bar	4	3	1	-	-	1	-	-	1	x	-	x	-	x
		Va	atm.	4	3	1	-	-	1	-	-	1	x	x	x	-	x
Rock dominated	120	Ib	atm.	(x)	-	-	-	-	-	-	(x)	2	-	-	-	-	-
		IIb	1 bar	4	-	-	-	-	2	-	(x)	1	x	-	x	-	-
	200	IIIb	atm.	4	-	-	1	-	1	-	-	1	x	-	x	-	-
		IVb	1 bar	4	2	-	-	-	1	1	-	1	x	-	x	-	-
		Vb	atm.	-	-	-	-	-	-	-	-	-	x	-	x	-	-
Saline	150	VI-0	atm.	4	-	-	-	2	1	-	-	2	-	-	x	-	-
		VI-1	atm.	4	-	3	-	-	1	-	-	1	x	-	x	-	-
		VI-2	atm.	4	-	3	-	-	1	-	-	1	x	-	x	x	x
		VI-4	atm.	4	-	3	-	-	1	-	-	1	x	-	x	x	x

Table 5. Concentrations of selected elements in reaction water (ppm), pH acquired at end of experiments, and calculated saturation indexes. Saturation indices (SI = log(Q/K), where Q is ion activity product and K is equilibrium constant) were calculated using PHREEQC v3. For experimental setup please see Table 2. * indicates analyses conducted by ICP-MS; the remaining values were acquired by colorimetric analysis.

Ex.	Na	Mg*	Al*	Cl	K	Ca	Si	Total Fe*	pH
Ia	168.50	0.03	0.24	27.80	6.41	31.90	157.78	0.09	10.4
IIIa	230.80	0.11	0.34	160.00	13.78	19.80	72.55	0.11	9.9
IIa	-	-	-	-	10.10	5.14	198.54	0.03	-
IVa	265.00	2.23	0.16	179.00	19.92	138.40	169.13	0.18	6.5

Calculated saturation index (SI)

Ex.	Analcime	Mordenite	Scolecite	Mg-saponite	Mg-nontronite	Clinochlore
Ia	9.67	8.29	25.29	11.77	36.3	5.58
IIIa	6.40	3.62	18.40	12.46	21.44	5.37
IVa	9.78	11.91	23.77	9.58	33.59	1.31

Ex.	Calcite	Aragonite	Dolomite	Siderite	Quartz
Ia	2.19	2.10	1.67	-12.53	-1.38
IIIa	3.40	3.34	-0.14	-15.76	-1.79
IVa	1.17	1.11	-1.98	-4.53	-0.20

Table 6. Estimatet *in situ* gas partial pressures (atm.), dissolved inorganic carbon (DIC, mmol/kgw) and pH in the reactor experiments. Values were calculated with PHREEQC v3 using the built-in Soave-Redlich-Kwong Equation of State (EoS), and a fixed head-space volume flash algorithm. The calculations used a water volume of 100 ml, and a head-space volume of 500 ml, representing the 600 ml Parr reactor.

	Exp.	MilliQ water, Air	MilliQ water, CO_2, H_2O	Seawater, Air	Seawater, CO_2, H_2O
25°C*	P_{H2O}	0.03	0.03	0.03	0.03
	P_{CO2}	$4e^{-4}$	0.85	$4e^{-4}$	0.86
	P_{N2}	0.78	-	0.78	-
	P_{O2}	0.21	-	0.21	-
	DIC	$1.6e^{-2}$	29.00	$1.3e^{-3}$	$2.7e^{-2}$
	pH	5.61	3.95	8.22	4.99
120°C**	P_{H2O}	1.97	1.97	1.93	1.94
	P_{CO2}	$7e^{-4}$	1.22	0.003	1.22
	P_{N2}	1.02	-	1.02	-
	P_{O2}	0.27	-	0.27	-
	DIC	$6.3e^{-3}$	11.00	$8.8e^{-4}$	$1.2e^{-4}$
	pH	5.79	4.25	7.60	5.52
150°C**	P_{H2O}	4.74	4.74	4.64	4.65
	P_{CO2}	$9e^{-4}$	1.30	0.006	1.30
	P_{N2}	1.08	-	1.08	-
	P_{O2}	0.29	-	0.29	-
	DIC	$5.74e^{-3}$	11.000	$4.6e^{-4}$	$1.2e^{-2}$
	pH	5.74	4.36	7.22	5.69
200°C**	P_{H2O}	15.5	15.5	15.16	15.16
	P_{CO2}	0.001	1.38	0.01	1.39
	P_{N2}	1.15	-	1.15	-
	P_{O2}	0.31	-	0.31	-
	DIC	$5.96e^{-3}$	12.00	$1.4e^{-4}$	$1.3e^{-2}$
	pH	5.64	4.57	6.55	5.76

*Initial condition in the reactor

**Condition after heating up the reactor from the initial conditions (25°C)

LIST OF FIGURES

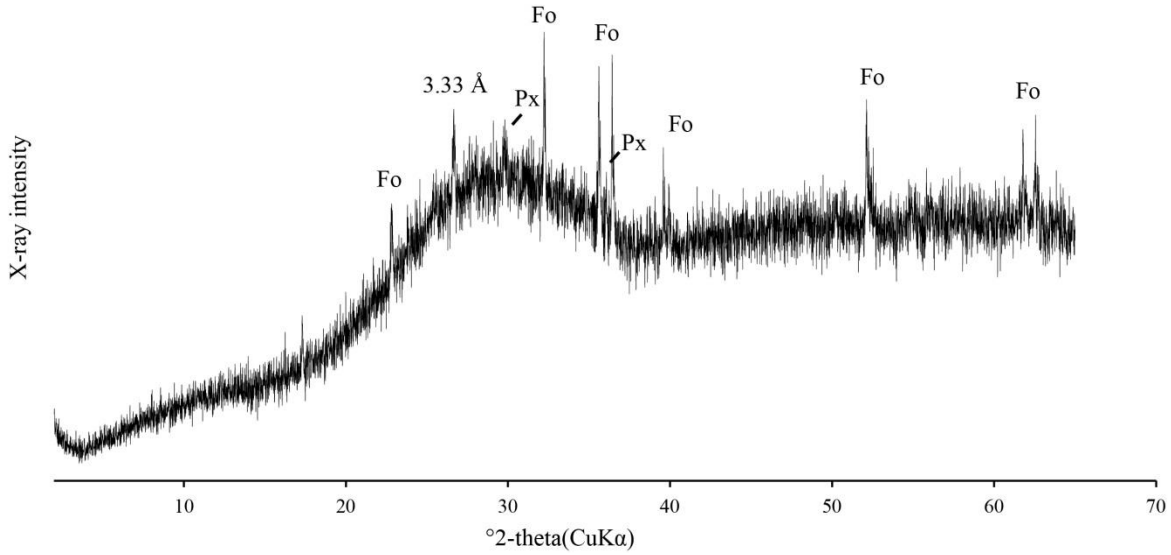

Figure 1. Diffractogram of original unaltered basalt. Fo: forsterite, Px: pyroxene, and unidentified mineral at 3.33 Å.

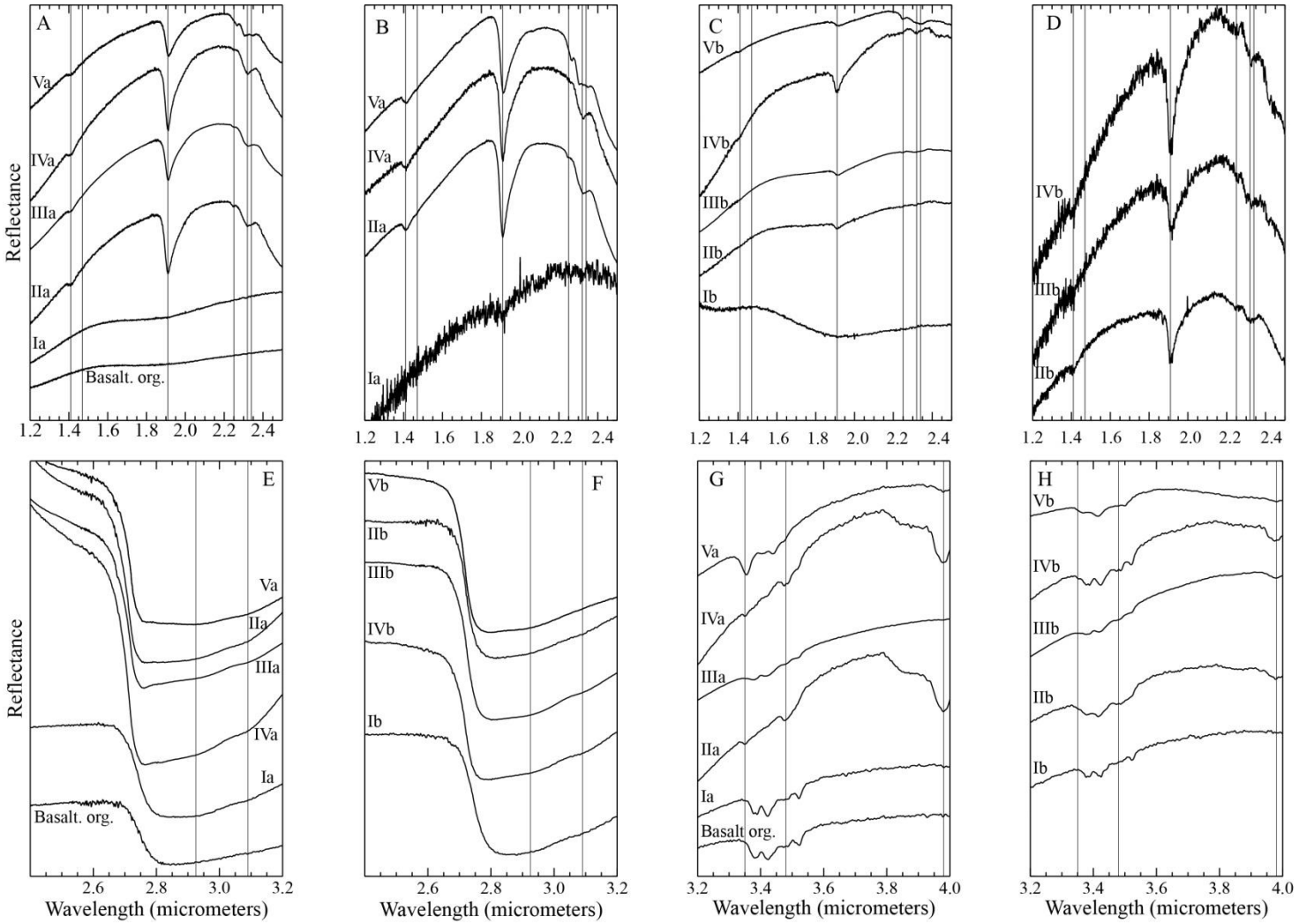

Figure 2. Reflectance spectra of the different experiments. Wavelength between 1.2 and 2.5 µm: A) fluid-dominated, B) fluid-dominated ratioed, C) rock-dominated and D) rock-dominated ratioed, with positions of selected absorption features at 1.41 µm, 1.47 µm, 1.91 µm, 2.25 µm, 2.32 µm, 2.34 µm are represented with lines. Wavelength between 2.4 and 3.2 µm: E) fluid-dominated and F) rock-dominated. Wavelengths between 3.2 and 4.0 µm: G) fluid-dominated between and H) rock-dominated. Positions of selected absorption features at 2.925 µm and 3.09 µm (E and F), and 3.35 µm, 3.48 µm and 3.98 µm (G and H) are represented with lines. Spectra are scaled and offset for clarity.

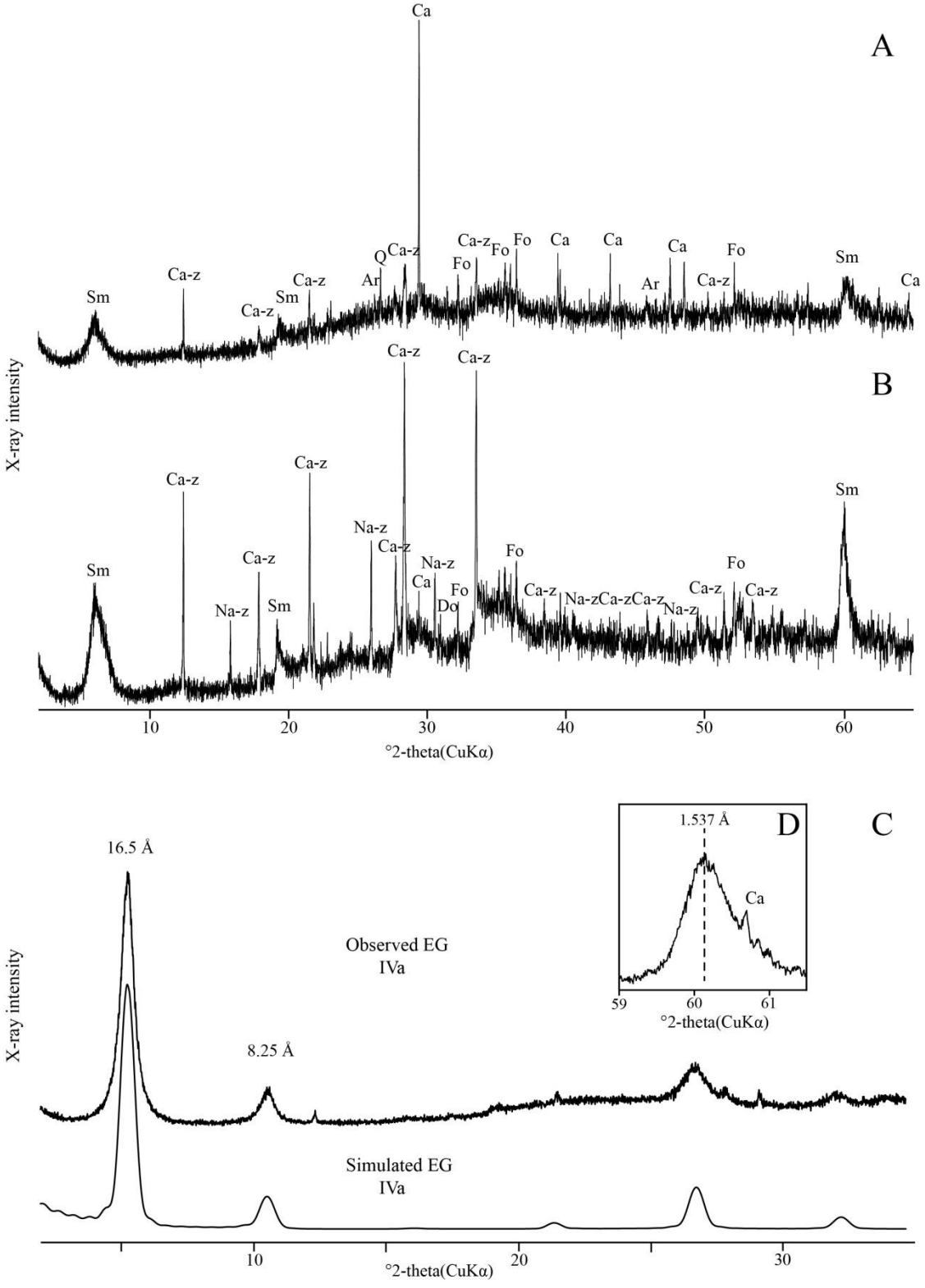

Figure 3. Selected XRD diffractograms. Whole rock XRD diffractogram of (A) IVb and (B) IIIa. (C) Observed (upper) and simulated (bottom) EG treated clay fraction diffractogram and randomly oriented (060) peak (D) for IVa. Na-z: Na-zeolite, Ca-z: Ca-zeolite, Ar: aragonite, Ca: calcite, Fo: forsterite, Sm: smectite.

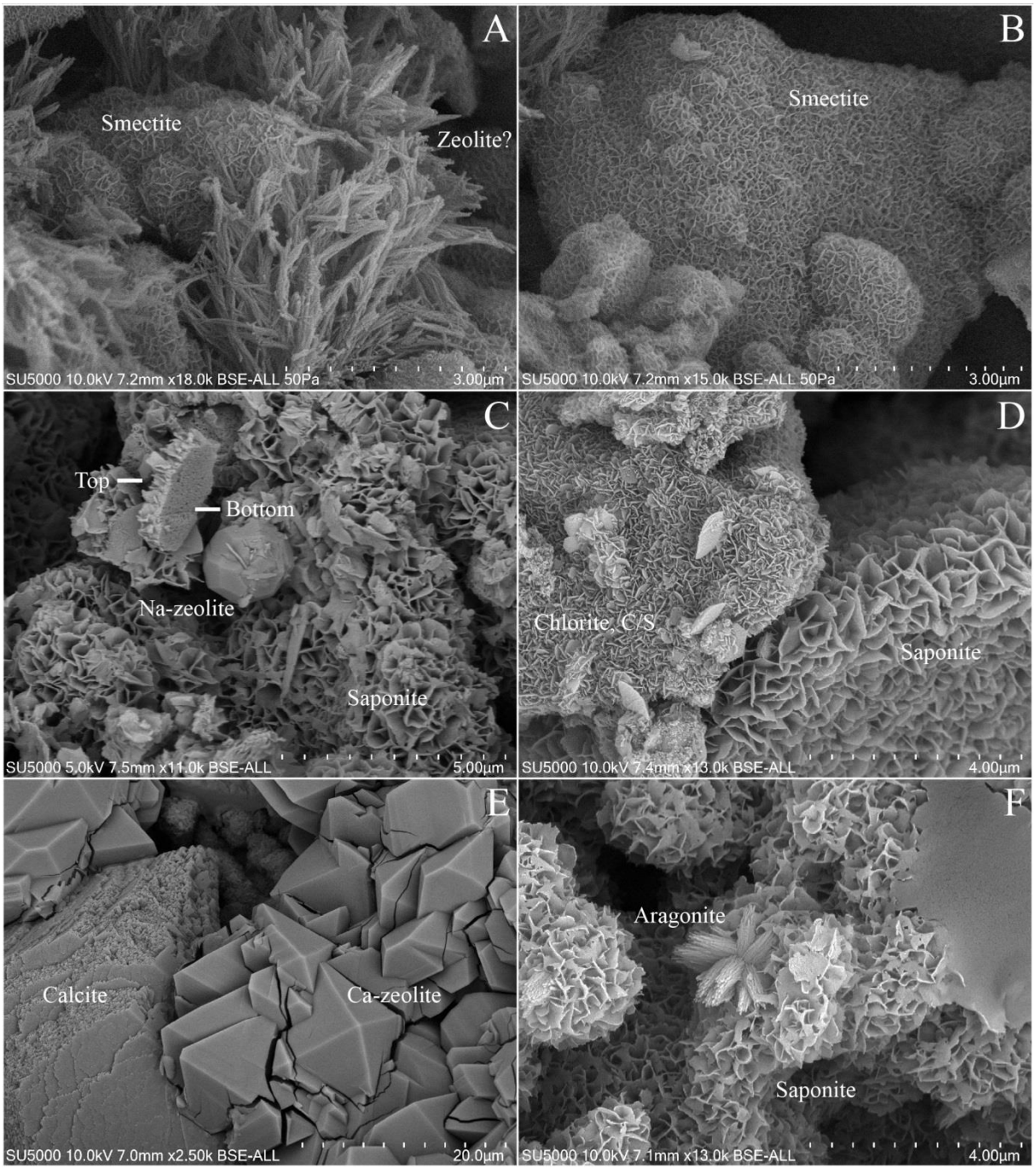

Figure 4. Selected SEM images displaying alteration phases. A) Possible zeolites and clay minerals (B) phase in Ib. C) Na-zeolite and smectite in sample IIIa. D) Accumulation of chlorite crystals and smectite in sample IIIb. E) Large calcite seemingly overgrown by Ca-zeolite, from sample IVb. F) Aggregation of prismatic aragonite crystals and smectite from IVb.

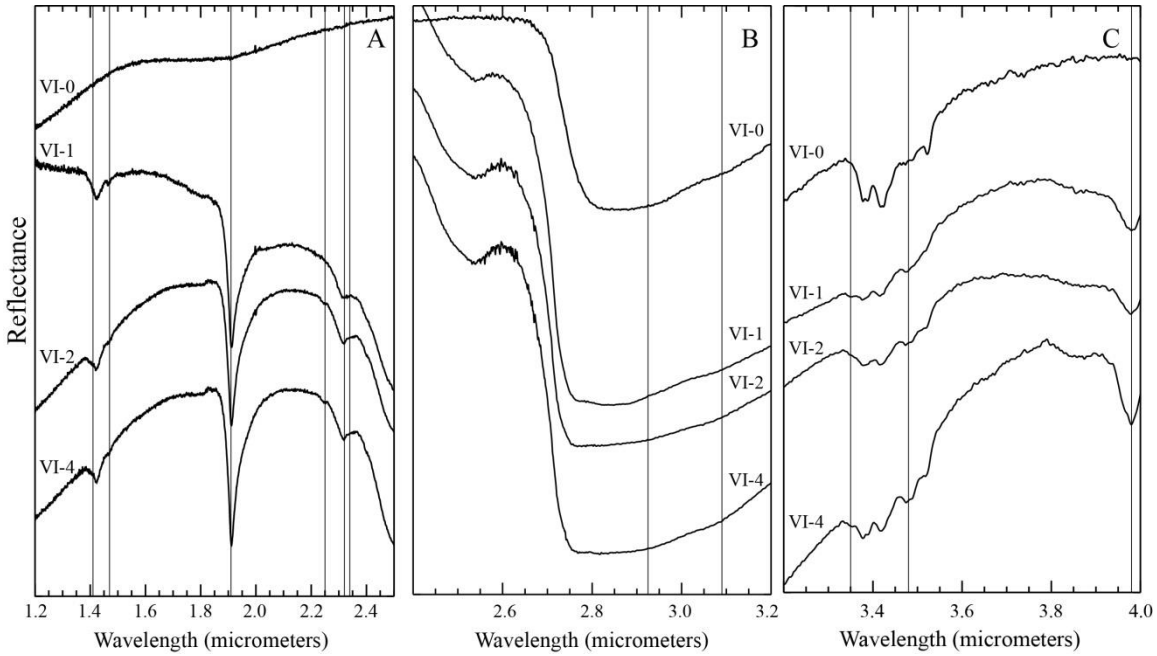

Figure 5. Reflectance spectra of the different saline experiments between: A) 1.2 and 2.5 µm, B) 2.4 and 3.2 µm and C) 3.2 and 4 µm. Positions of selected absorption features: A) 1.41, 1.47, 1.91, 2.25, 2.32 and 2.34 µm, B) 2.925 and 3.09 µm, C) 3.35, 3.48 and 3.98 µm are represented with lines.

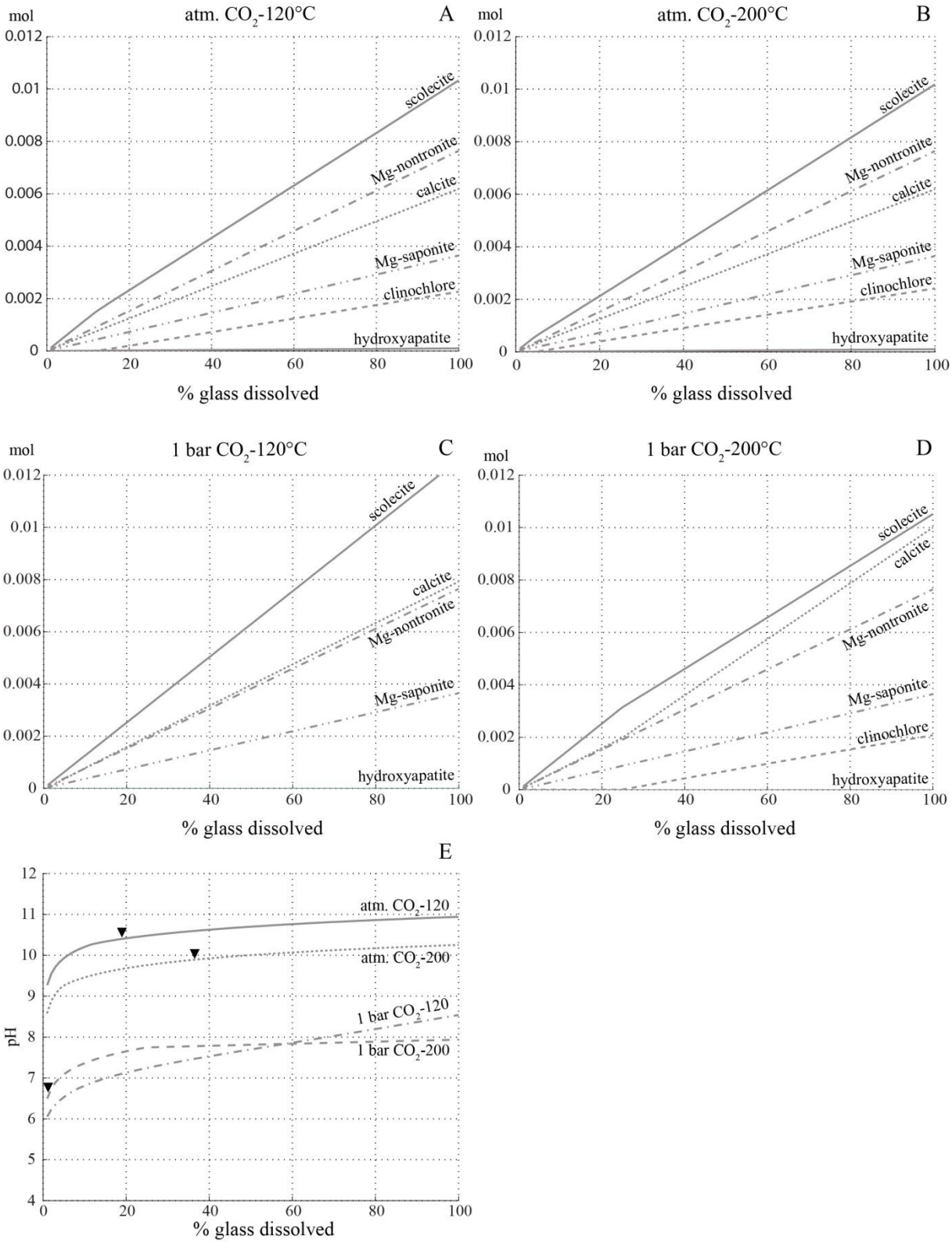

Figure 6. Minerals predicted to form in reaction path model. Upper images are of model set up with atmospheric CO_2 for 120°C A) and 200°C B). The middel images are of model set up using 1 bar CO_2 and 120°C C) and 200°C D). Y-axis shows mole minerals formed per 100 ml aqueous solution. Image D) shows predicted pH the various experiments. Triangle marks the measured pH at end of experiment.